JGR Space Physics

RESEARCH ARTICLE
10.1029/2023JA032257

Relativistic Electron Precipitation Events Driven by Solar Wind Impact on the Earth's Magnetosphere

Alexandra Roosnovo[1], Anton V. Artemyev[2], Xiao-Jia Zhang[2,3], Vassilis Angelopoulos[2], Qianli Ma[4,5], Niklas Grimmich[6], Ferdinand Plaschke[6], David Fischer[7], and Magnes Werner[7]

[1]ISR Space Science and Applications Group, Los Alamos National Laboratory, Los Alamos, NM, USA, [2]Department of Earth, Planetary, and Space Sciences, University of California, Los Angeles, CA, USA, [3]Department of Physics, University of Texas at Dallas, Richardson, TX, USA, [4]Department of Atmospheric and Oceanic Sciences, University of California, Los Angeles, CA, USA, [5]Center for Space Physics, Boston University, Boston, MA, USA, [6]Institut für Geophysik und Extraterrestrische Physik, Technische Universität Braunschweig, Braunschweig, Germany, [7]Space Research Institute, Austrian Academy of Science, Graz, Austria

Key Points:

- A corotating interaction region (CIR) and interplanetary coronal mass ejection (ICME), both including interplanetary shocks, are observed resulting in relativistic electron precipitation from low-altitude orbit
- Duskside precipitation after CIR impact is driven by intense electromagnetic ion cyclotron waves, showing distinct energy-L dispersion from magnetic field distortion
- Dawnside precipitation after ICME impact is driven by intense whistler-mode waves resonating with electrons at high latitudes

Correspondence to:

A. Roosnovo,
aroosnovo@lanl.gov

Citation:

Roosnovo, A., Artemyev, A. V., Zhang, X.-J., Angelopoulos, V., Ma, Q., Grimmich, N., et al. (2024). Relativistic electron precipitation events driven by solar wind impact on the Earth's magnetosphere. *Journal of Geophysical Research: Space Physics*, *129*, e2023JA032257. https://doi.org/10.1029/2023JA032257

Received 3 NOV 2023
Accepted 3 APR 2024

Abstract

Certain forms of solar wind transients contain significant enhancements of dynamic pressure and may effectively drive magnetosphere dynamics, including substorms and storms. An integral element of such driving is the generation of a wide range of electromagnetic waves within the inner magnetosphere, either by compressionally heated plasma or by substorm plasma sheet injections. Consequently, solar wind transient impacts are traditionally associated with energetic electron scattering and losses into the atmosphere by electromagnetic waves. In this study, we show the first direct measurements of two such transient-driven precipitation events as measured by the low-altitude Electron Losses and Fields Investigation CubeSats. The first event demonstrates storm-time generated electromagnetic ion cyclotron waves efficiently precipitating sub-relativistic and relativistic electrons from >300 keV to 2 MeV at the duskside. The second event demonstrates whistler-mode waves leading to scattering of electrons from 50 to 700 keV on the dawnside. These observations confirm the importance of solar wind transients in driving energetic electron losses and subsequent dynamics in the ionosphere.

1. Introduction

The dynamics of the Earth's magnetosphere, especially those of the Earth's inner magnetosphere, are largely controlled by solar wind impacts (Kivelson & Russell, 1995). The most intense and sudden types of impact are those which include interplanetary (IP) shock waves, which result from the interaction of fast and slow solar wind streams and manifest as the upstream shock structures accompanying the larger geoeffective solar wind transient phenomena, such as IP coronal mass ejections (ICMEs) and corotating interaction regions (CIRs) (Gopalswamy et al., 2003; Gosling, 1996; Heber et al., 1999; Nitta et al., 2021; Richardson, 2018). Such impacts have the ability to trigger rapid, large-scale redistribution of energetic particle fluxes in the radiation belts (e.g., Blake et al., 1997; Lyons et al., 2005; Tsurutani et al., 1995, 2011). This redistribution involves significant adiabatic effects related to magnetic field reconfiguration, as well as kinetic effects related to plasma wave generation and energetic particle scattering.

The impact of the strongly intensified solar wind dynamic pressure that is characteristic to large-scale solar wind transients (sometimes seen as distinct pulses of augmented pressure) compresses the Earth's dayside magnetosphere and has an immediate influence on charged particle dynamics. This includes the formation of unstable (anisotropic) particle velocity distributions (e.g., X. X. Zhao et al., 2022, and references therein) as well as electron flux dropouts and enhancements (e.g., Da Silva et al., 2023; X. H. Ma et al., 2021). The basic mechanism for the formation of unstable particle distributions consists of the adiabatic heating of ions and electrons via induction electric fields. Such heating is usually more effective for equatorial particles, resulting in the formation of perpendicularly anisotropic particle populations which are unstable to whistler-mode waves (see Kennel, 1966; Sagdeev & Shafranov, 1961) and electromagnetic ion cyclotron (EMIC) waves (see, e.g., Liu et al., 2022; Thorne & Kennel, 1971; Yan et al., 2023; Zuxiang et al., 2023).

Indeed, in-situ spacecraft measurements have detected many cases of whistler-mode chorus (e.g., C. Zhou et al., 2015; X. Zhou et al., 2023) and EMIC wave (e.g., Usanova et al., 2012) generation in response to solar wind dynamic pressure increases such as those which occur during an IP shock wave's arrival to the Earth's magnetosphere. A detailed multi-case study by Yue et al. (2017) demonstrated that IP shock impact can significantly increase the intensity of whistler-mode chorus waves in the outer radiation belt, outside of the plasmapause. Although this type of wave intensity enhancement is typical for any positive pulses (i.e., increases) of the solar wind dynamic pressure, IP shocks often provide the strongest effect (Jin et al., 2022). Interestingly, wave intensity increases not only around the equatorial plane, where the chorus generation region is located (see reviews by Tao et al. (2020), Omura (2021), and references therein), but in low-altitude regions as well (Bezděková et al., 2021). This suggests that the more intense whistler-mode waves driven by IP shock impact are not damped by suprathermal electron fluxes (Bortnik et al., 2007; L. Chen et al., 2013) and can propagate to high latitudes, thus significantly increasing their global efficiency in scattering relativistic electrons (see discussion in L. Chen et al. (2021, 2022) and Artemyev et al. (2021)).

Magnetospheric impact by strong solar wind transient IP shocks plays a similarly significant role in the intensification of EMIC waves (Yan et al., 2023). Blum et al. (2021) described a CME event that led to a series of compressions of the dayside magnetosphere by pulses of solar wind dynamic pressure; each of such compressions resulted in proton adiabatic heating and near-equatorial EMIC wave generation. The effects of EMIC wave generation due to IP shock impact on the Earth's magnetosphere can be even more evident, such as in the stark ion flux enhancements observed by Y.-X. Li et al. (2022) and Zuxiang et al. (2023). Moreover, EMIC wave intensity enhancements in response to solar wind pulses may also be observed simultaneously on the day and night sides of the Earth, as when coinciding with plasma sheet ion injections driven by substorm activities (Xue et al., 2022; Yan et al., 2023). For EMIC wave generation in particular, the solar wind impact may consist of two independent processes: (a) direct proton heating by magnetic field compression within the inner magnetosphere and (b) injection of hot, anisotropic protons into the inner magnetosphere by flow bursts and dipolarizing flux bundles arising from localized reconnection in the magnetotail (see discussion and comparison of these two processes in, e.g., H. Chen et al., 2020; Upadhyay et al., 2022).

Although whistler-mode and EMIC wave generation caused by IP shock waves and solar wind dynamic pressure pulses has been previously reported, as it is commonly observed by near-equatorial spacecraft, details on the influence of these waves on radiation belt dynamics have yet to be fully investigated. One expected effect of importance is the scattering and resultant precipitation of energetic electrons by intense whistler-mode and EMIC waves. However, such electron precipitation can only be observed by low-altitude spacecraft (i.e., taking advantage of finite, ~20°, pitch-angle resolution measurements of electron distributions within a large, i.e., many tens of degrees, loss cone) or ground-based measurements of X-ray emission (see, e.g., example in Breneman et al. (2020)). Direct measurements of precipitating electron fluxes in response to solar wind dynamic pressure enhancements can therefore be highly useful for understanding the importance of transients, including IP shocks, in magnetosphere-ionosphere coupling and radiation belt depletion.

Here, we describe two events in which large-scale solar wind structures impact the Earth's magnetosphere and drive sub-relativistic and relativistic electron losses. Both precipitation events were captured by the low-altitude measurements of the Electron Losses and Fields Investigation (ELFIN) CubeSats (Angelopoulos et al., 2020). The first event consists of a magnetospheric impact by a CIR (with an embedded IP shock and prominent solar wind discontinuities) that drives a magnetospheric storm and strong sub-relativistic and relativistic electron precipitation by EMIC waves on the duskside; the second event consists of a separate ICME impact, adjoined by a prominent IP shock, that drives strong energetic electron precipitation, extending to relativistic energies, by whistler-mode waves on the dawnside. We describe the satellite observations of the solar wind, inner magnetosphere, and low-altitude space region in Section 2. In Sections 2.1 and 2.2, we examine the first and second events, respectively. In Section 3, we discuss our results and the likely characteristics of the specific waves responsible for the two electron precipitation events. Finally, we summarize our results and present conclusions in Section 4.

2. Observations

We examine two specific events of electron precipitation, observed from the low-altitude vantage point of ELFIN, driven by IP shock interaction with the terrestrial magnetosphere: the first event (S#1) occurred on 6 March 2021, and the second event (S#2) occurred on 12 May 2021. We use ELFIN observations of precipitating (inside the local bounce loss cone) and locally trapped (outside the local bounce loss cone) fluxes within the 16-channel energy range of 50–6,000 keV at 1.5 s time resolution (half the ELFIN spin rate and sufficient to collect the full pitch-angle, energy distribution) (Angelopoulos et al., 2020). We also use the precipitating-to-trapped flux ratio as an effective measure of the intensity of electron precipitation (see examples in Mourenas et al., 2021; Tsai et al., 2022; Zhang, Artemyev, et al., 2022).

To monitor the solar wind and magnetospheric conditions for perturbations indicative of transient and accompanying shock arrival, we utilize observations from the Time History of Events and Macroscale Interactions during Substorms (THEMIS) mission and The Geostationary Operational Environmental Satellite (GOES). Measurements of the upstream solar wind, where an approaching IP shock is first observable as a sharp gradient of solar wind velocity and magnetic field magnitude, are taken from the Acceleration, Reconnection, Turbulence, and Electrodynamics of the Moon's Interaction with the Sun (ARTEMIS) subset of THEMIS spacecraft (specifically, ARTEMIS P2 also know as THEMIS C, with the latter designation utilized hereafter). The ARTEMIS satellites orbit the moon and measure the solar wind magnetic field (Auster et al., 2008) and plasma (Artemyev et al., 2018; McFadden et al., 2008). The three other THEMIS spacecraft (A, D, and E) orbit the Earth with an apogee of $\sim 12R_E$ (Angelopoulos, 2008). We use THEMIS A magnetic field and plasma measurements (3–4 s spin resolution) to monitor the near-Earth dayside magnetosheath and foreshock response to the arriving IP shock. Additionally, to identify plasma injections we check energetic ion and electron measurements made by the GOES-16 and GOES-17 space weather suite of instruments (Boudouridis et al., 2020; Dichter et al., 2015). Figure 1 shows the orbits of THEMIS, GOES, and ELFIN spacecraft relative to the modeled nominal magnetopause and bow shock (King & Papitashvili, 2005; Shue et al., 1997; Wu et al., 2000), as well as the geomagnetic activity, as represented by Sym-H and AE indices, around the time of each event.

2.1. First Event: EMIC Wave-Driven Precipitation

Our first event occurred on 6 March 2021. Figure 2 shows an overview of THEMIS C and THEMIS A observations. THEMIS C observes the large-scale solar wind perturbations of a CIR (see Gosling, 1996; Heber et al., 1999; Richardson, 2018), starting at ~ 01:00 UT with a slight jump of solar wind speed (panel (b)). Simultaneous variations of magnetic field magnitude (panel (a)) and plasma density (panel (b)) show the series of rotational discontinuities (rotation of $\mathbf{B}$ components with $|\mathbf{B}| \approx const$) associated with an IP shock wave embedded in a CIR (see detailed discussion in Gosling (1996)). Distinct from the initial fine structure of solar wind perturbations, the large scale magnetic field and solar wind discontinuities, seen prominently in the ion spectra variation around 05:40–06:00 UT in panel (d), are expected to compress the Earth's magnetosphere and drive a geomagnetic storm (see Alves et al., 2006; Gonzalez et al., 1999). Indeed, Sym-H and AE indexes in Figure 1 show moderately depressed Sym-H, indicative of storm-like activity, along with so-called high-intensity, long-duration, continuous AE activity (as described in Tsurutani et al. (2004, 2006)). Activity starts with magnetosphere compression from 01:00–02:00 UT (positive Sym-H) and continues to a moderately negative Sym-H of around −20 nT with recurrent substorms (AL minimum reaching ~−800 nT). The substorm around 03:00 UT is associated with a strong ion injection observed at GOES-16 in the pre-midnight sector (not shown). Such events are usually characterized by an increased level of relativistic electrons in the inner magnetosphere (Hajra et al., 2014, 2015), but have not been studied in the context of relativistic electron precipitation.

Overlapping with THEMIS C observations of the CIR, THEMIS A, located inside the compressed magnetosheath (see Figure 1), detects multiple strong magnetic field perturbations accompanied by density variations and hot magnetospheric plasma bursts, starting at ~05:40 UT and continuing to a little before ~09:00 UT. Such variations of density and cold/hot plasma flux are indicative of multiple magnetopause crossings due to magnetopause surface waves (e.g., Agapitov et al., 2009; Archer et al., 2019) or Kelvin-Helmholtz waves (e.g., Hasegawa et al., 2004). B_z changes sign multiple times, indicating that the magnetosheath is filled by negative polarity B_z variations that potentially drive magnetopause reconnection (Burch et al., 2016; Paschmann et al., 1979, 2013; Phan et al., 2014); multiple plasma jets (v_z excursions from the ambient sheath flow) are also seen. Thus, THEMIS A confirms the strong driving of the Earth's magnetosphere by the CIR after its arrival between ~01:00 UT and ~06:00 UT.

At ~06:47 UT, near the time of the observed Sym-H minimum (1 hr after THEMIS C detects the ending edge of the CIR with a large increase of the solar wind speed), and still well within the prolonged, albeit weak, storm main phase, ELFIN A crosses the dusk flank (MLT ~ 18) and observes strong precipitation of both sub-relativistic (<500 keV) and relativistic (≥500 keV) electrons. Figure 3 shows an overview of flux observations capturing this precipitation. The precipitation burst covers a wide range of magnetic latitudes within the outer radiation belt,

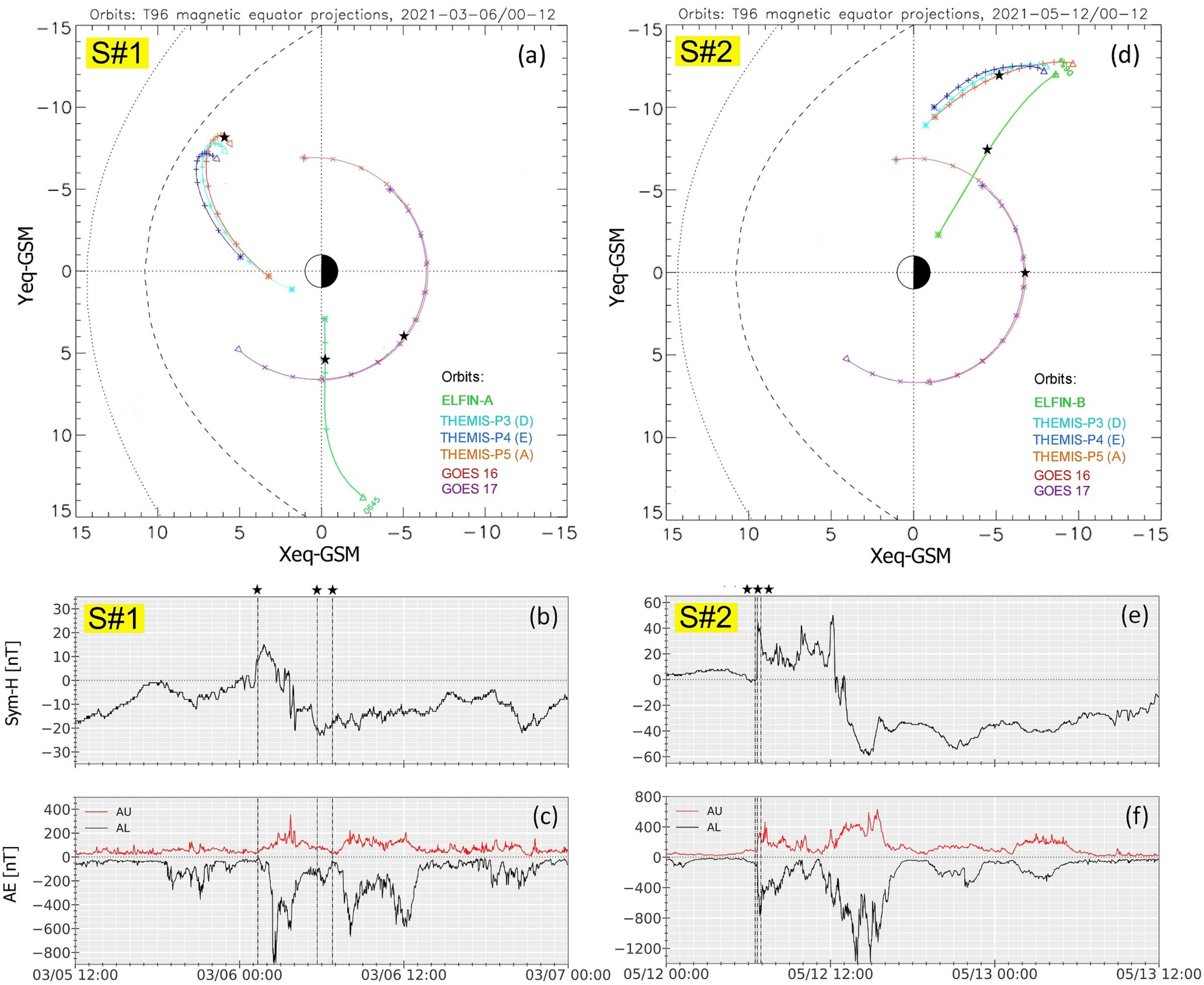

Figure 1. (a), (d) Equatorially projected positions of Time History of Events and Macroscale Interactions during Substorms (THEMIS), Geostationary Operational Environmental Satellite (GOES), and Electron Losses and Fields Investigation (ELFIN) spacecraft relative to the modeled nominal magnetopause (dashed curve) and bow shock (dotted curve). ARTEMIS (THEMIS B and C) is located in the solar wind, out of frame. For each orbit, the start time is marked with a triangle while the end time is marked with an asterisk; the tick marks between represent hour intervals for THEMIS and GOES satellites and minute intervals for ELFIN. The bottom panels show (b), (e) Sym-H and (c), (f) AE indexes for the 2-day interval encompassing each event. The orbits of observation and geomagnetic indices for the first event (S#1) are shown in the left panels, while those of the second event (S#2) are shown on the right. The stars mark the approximate locations and times for the different shock observations made by ARTEMIS, THEMIS, and ELFIN.

$MLAT \in [61.4, 59.4°]$ (corresponding to a wide L-shell range in the equatorial region of electron scattering, $\Delta L \sim 1$), between the plasma sheet region (before 06:47:15 UT; region with only <300 keV electron fluxes; see detailed analysis of such ELFIN observations in, e.g., Artemyev et al., 2022) and plasmasphere (after 06:48:30 UT; region with characteristic depletion of $\sim 100-200$ keV fluxes due to scattering by plasmaspheric hiss waves; see detailed analysis of such ELFIN observations in, e.g., Mourenas et al., 2021).

Panel (c) of Figure 3 displays the precipitating-to-trapped flux ratio, an important characteristic of the electron precipitation pattern that allows association with specific electron scattering mechanisms (see discussion in Angelopoulos et al. (2023)). The precipitating-to-trapped electron flux ratio for S#1 maximizes above 1 MeV and remains around ~1 (the strong diffusion limit; see Kennel, 1969) for energies $2-3$ MeV. This ratio decreases as energy decreases, dropping to ~0.1 below ~300 keV but remaining well above zero down to 50 keV. The precipitating-to-trapped flux ratio is inversely proportional to the pitch-angle diffusion rate, $D_{\alpha\alpha}$, evaluated around the loss cone (Kennel & Petschek, 1966; W. Li et al., 2013; Mourenas et al., 2021). Therefore, we can

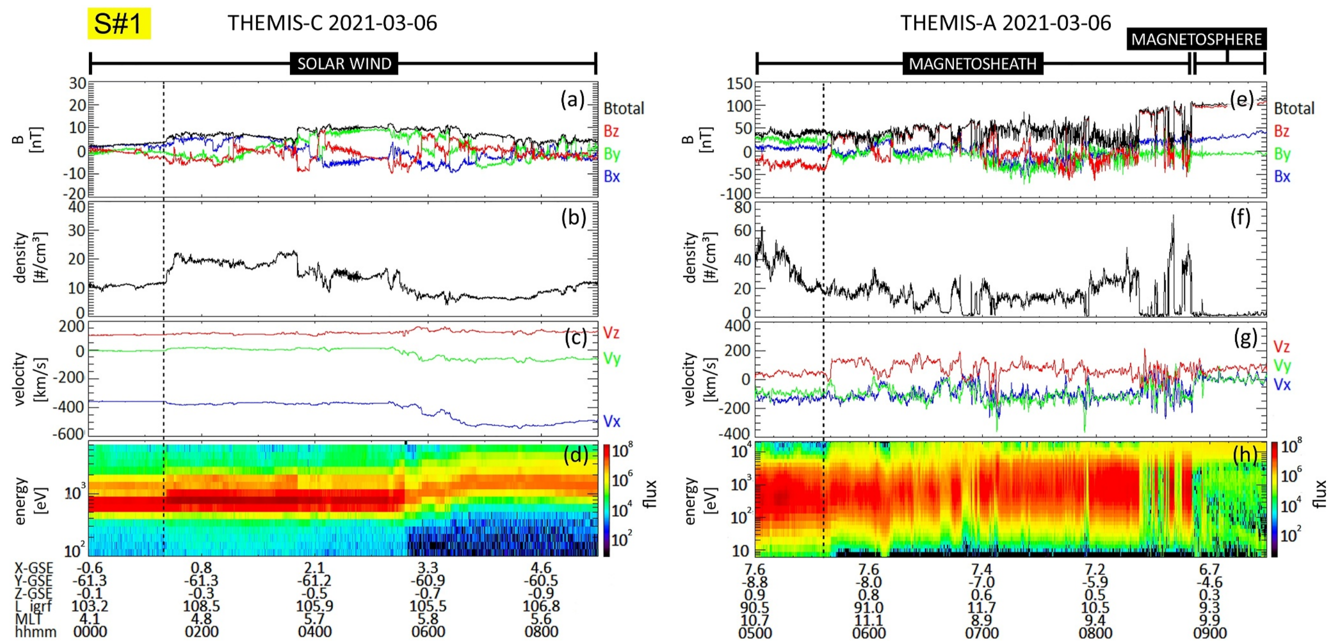

Figure 2. Overview of ARTEMIS (Time History of Events and Macroscale Interactions during Substorms (THEMIS C) and THEMIS A observations for event S#1 on 6 March 2021: THEMIS C (a) magnetic field, (b) plasma density, (c) plasma flow speed, and (d) ion energy spectrum and THEMIS A (e) magnetic field, (f) plasma density, (g) plasma flow speed, and (h) ion energy spectrum, with the colorbar showing flux in [cm^{-2} s^{-1} sr^{-1} eV^{-1}]. At the bottom of each set of panels (a–d, e–h) are location and time information, including the X, Y, and Z positions in the GSE coordinate system, L and MLT values, and the hour (hh) and minute (mm) for the day of the event. The beginning of the primary disturbances caused by the shock are indicated by the dashed lines across panels (a–d) and (e–h), as observed by THEMIS C and THEMIS A, respectively.

associate this energy profile of the precipitating-to-trapped flux ratio with an electron scattering mechanism that has (a) sufficiently large $D_{\alpha\alpha}$ above 1 MeV and (b) $D_{\alpha\alpha}$ that decreases with decreasing energy. Electron resonant scattering by EMIC waves has demonstrated such a $D_{\alpha\alpha}$ profile with large values at relativistic energies (Kersten et al., 2014; Ni et al., 2015; Summers & Thorne, 2003). In contrast, electron scattering by whistler-mode waves shows $D_{\alpha\alpha}$ maximizing below 100 keV (Albert, 2005; Glauert & Horne, 2005; Summers et al., 2007b), and thus for a whistler-mode scattering mechanism we would expect the precipitating-to-trapped flux ratio to maximize at low energies (see examples of ELFIN observations of whistler-driven precipitations in, e.g., Tsai et al., 2022; Zhang, Angelopoulos, et al., 2022). Previously published ELFIN observations of electron precipitation in conjunction with equatorial (An et al., 2022) and ground-based (Grach et al., 2022) observations of EMIC waves show the precipitating-to-trapped flux ratio maximizing at relativistic energies in a very similar pattern to that seen in Figure 3; statistical studies of EMIC wave-driven precipitation have further confirmed such a precipitating-to-trapped flux ratio pattern as being characteristic to EMIC-wave driving (Angelopoulos et al., 2023; Capannolo et al., 2023).

Meanwhile, GOES-17, located in the pre-midnight sector, observes a strong B_z depletion of ∼−50 nT (not shown) that is associated with a ring current injected ion population (Daglis et al., 1999), the principal source of EMIC waves (e.g., L. Chen et al., 2010, 2011). The duskside location of the precipitation event further supports characterization as EMIC-driven scattering, as this is the primary region of EMIC wave generation, with aforementioned hot plasma sheet (ring current) ions drifting duskward after being injected at the nightside (Jun et al., 2019, 2021; Thorne & Kennel, 1971). We note, however, that the large precipitating-to-trapped flux ratio (∼0.1) below 300 keV observed in this precipitation event is theoretically challenging for models describing electron precipitation solely by EMIC waves (see discussion in Hendry et al. (2019), Capannolo, Li, Ma, Chen, et al. (2019), and Capannolo, Li, Ma, Shen, et al. (2019)). In the Discussion section, we provide a brief overview of effects that could potentially decrease the electron precipitating energies for an EMIC event, resulting in spectra similar to that observed in S#1.

Although there was no direct magnetic conjunction of ELFIN with near-equatorial spacecraft during the first event, the geostationary GEO-KOMPSAT-2A (Seon et al., 2020) satellite was traveling along the dusk flank around the

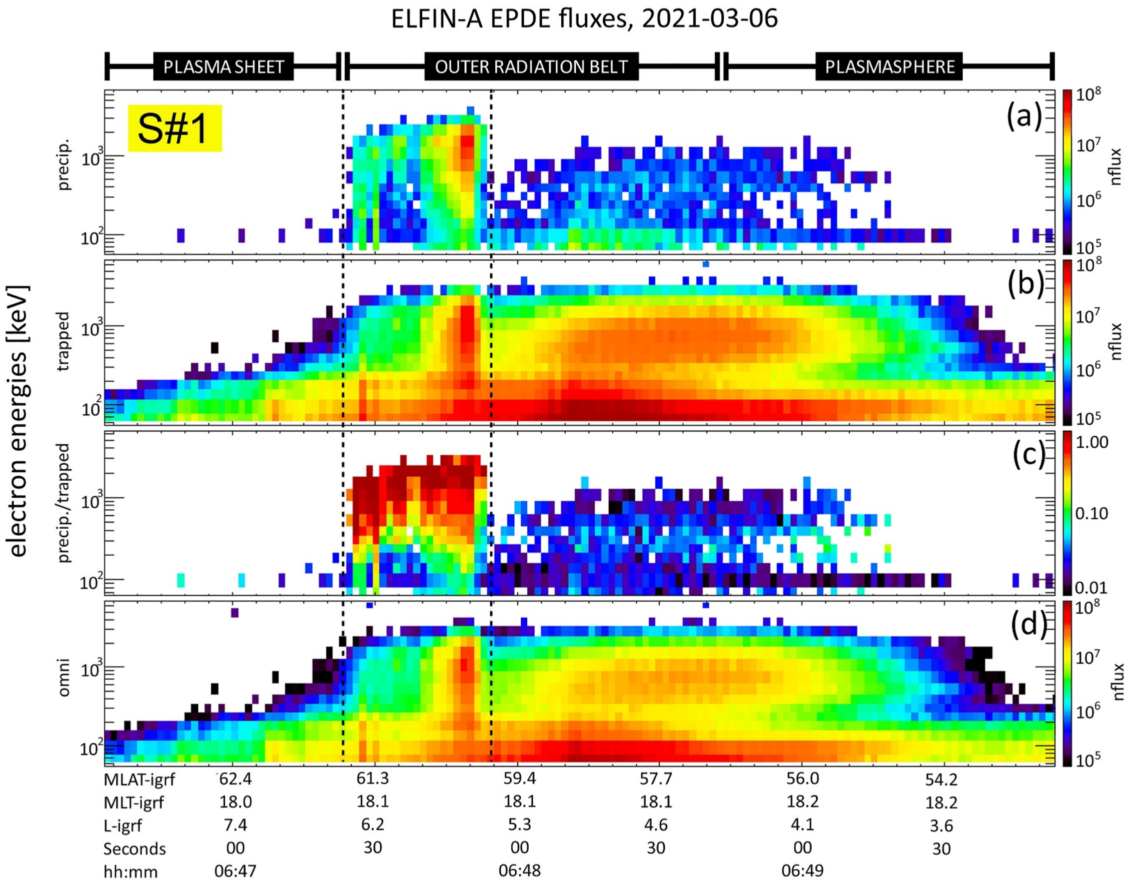

Figure 3. Overview of Electron Losses and Fields Investigation observations for event S#1 on 6 March 2021: (a) precipitating electron fluxes, (b) trapped fluxes, (c) precipitating-to-trapped flux ratios, and (d) omnidirectional fluxes. In panels (a), (b), and (d) the colorbar shows flux in [cm^{-2} s^{-1} sr^{-1} MeV^{-1}]. The dashed lines demarcate the time interval in which electron precipitation is primarily observed, as indicated in the enhancement of the precipitating-to-trapped ratio (i.e., ratio approaches unity).

time of ELFIN electron precipitation observations and observed several intense bursts of helium band EMIC waves. Figure 4 shows KOMPSAT fluxgate magnetometer measurements (1 s resolution; Constantinescu et al., 2020; Magnes et al., 2020) during the interval of 05:00–09:00 UT. There are clear EMIC wave bursts (bottom panel) around 05:10, 06:10, and 08:00–09:00 UT, covering an MLT range that extends from 13 up to 18. These time intervals and MLT locations do not exactly overlap with ELFIN measurements at ~06:50 UT, MLT ~ 18, but do provide a useful context for ELFIN measurements. KOMPSAT shows that a large part of the dusk flank is filled by EMIC wave source regions at the times surrounding our observations; these regions can survive for a long time and be quite extended in MLT (Blum et al., 2020; Engebretson et al., 2015; Hendry et al., 2020). Thus, the observation of multiple EMIC wave source regions in close spatial and temporal proximity to ELFIN observations of electron precipitation follows our interpretation of EMIC wave scattering. Although KOMPSAT does not provide plasma measurements with which we could directly evaluate wave generation for this event, multiple previous studies have demonstrated that dusk-sector EMIC waves are generated by ring-current ions injected from the plasma sheet (L. Chen et al., 2009, 2010; Lubchich & Semenova, 2015; Min et al., 2015) or through magnetospheric compression by the solar wind (e.g., Jun et al., 2024); it is likely that the second scenario is realized in this event.

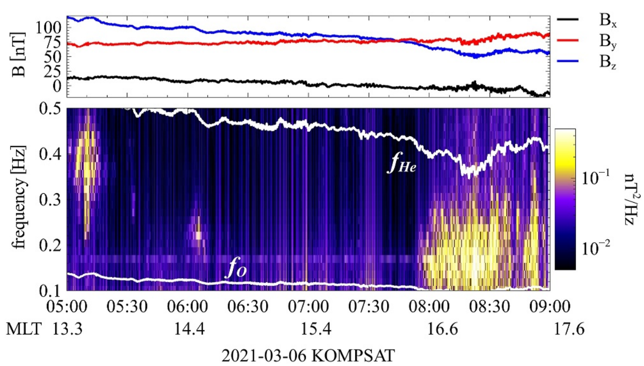

Figure 4. An overview of KOMPSAT magnetic field measurements at the dusk flank around the time of event 1: magnetic field components (top panel) and magnetic field spectrum for electromagnetic ion cyclotron wave frequency range (bottom panel). The two white lines depict helium (He) and oxygen (O) gyrofrequencies.

Interestingly, EMIC wave-driven precipitation is quite long lasting (multiple ELFIN spins covering almost $\Delta L \sim 1$ and reaching the upper limit of the

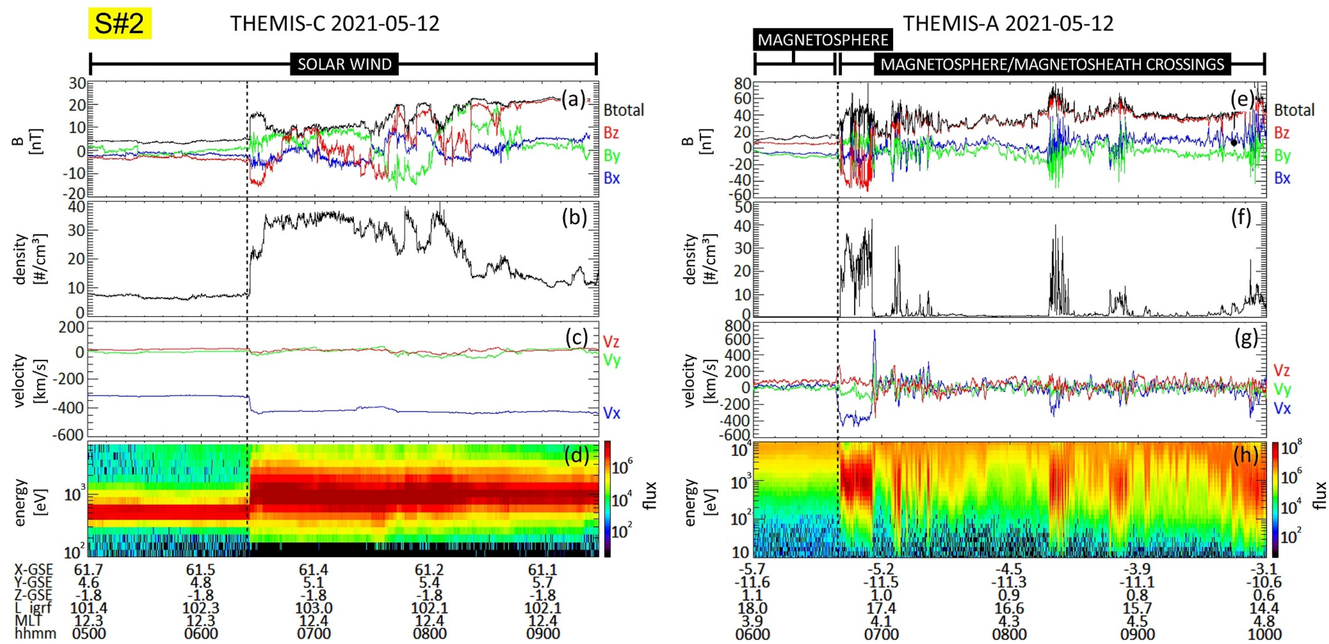

Figure 5. Overview of ARTEMIS (Time History of Events and Macroscale Interactions during Substorms (THEMIS C) and THEMIS A observations for event 2 on 12 May 2021: THEMIS C (a) magnetic field, (b) plasma density, (c) plasma flow speed, and (d) ion energy spectrum and THEMIS A (e) magnetic field, (f) plasma density, (g) plasma flow speed, and (h) ion energy spectrum, with the colorbar showing flux in [cm^{-2} s^{-1} sr^{-1} eV^{-1}]. At the bottom of each set of panels (a–d, e–h) are location and time information, including the X, Y, and Z positions in the GSE coordinate system, L and MLT values, and the hour (hh) and minute (mm) for the day of the event. The beginning of the primary disturbances caused by the shock are indicated by the dashed lines across panels (a–d) and (e–h), as observed by THEMIS C and THEMIS A, respectively.

range of sizes expected for an equatorial EMIC wave source region (Blum et al., 2016, 2017)). Our first event additionally includes two types of dE/dL (or $dE/dMLAT$) gradients: one around 06:47:30 UT, with the minimum precipitating electron energy increasing as L-shell decreases ($dE/dL < 0$), and a second around 06:47:45 UT, when the minimum precipitating electron energy decreases as L-shell decreases ($dE/dL > 0$). The dE/dL gradient is likely provided by the dependence of the minimum resonance energy on the equatorial ratio of the plasma frequency and the gyrofrequency, $E \propto f_{ce}/f_{pe}$ (Summers & Thorne, 2003). In the unperturbed dipole magnetic field $f_{ce} \propto L^{-3}$ and $f_{pe} \propto L^{-2}$ (see the empirical model in Sheeley et al. (2001)), which will give $E \propto L^{-1}$ with $dE/dL < 0$ (observed at larger L, around 06:47:30 UT). Substorm injections, however, transport hot ion populations (Birn et al., 2015; Gkioulidou et al., 2014, 2016; Ukhorskiy et al., 2017, 2018) that may form localized regions of magnetic field depletion (so-called magnetic dips, Xia et al., 2019; Zhu et al., 2021) filled by EMIC waves (see He et al., 2017; Yin et al., 2022; Yu et al., 2023; Y. Zhao et al., 2023). This magnetic field depletion will result in a weaker radial gradient of f_{ce}, that is $f_{ce} \propto L^{-3+q}$ with $q > 0$ (Xia et al., 2019; Zhu et al., 2021), and this effect may make $f_{ce}/f_{pe} \propto L^{-1+q}$ increase with decreasing L (i.e., $dE/dL > 0$, observed around 06:47:45 UT). Therefore, the inverse gradient of the precipitating energies ($dE/dL > 0$, seen in Figure 3) corroborates the hypothesis that here a strong ion injection is penetrating deep into the plasmapause and driving significant losses of sub-relativistic and relativistic electrons. Indeed, KOMPSAT magnetic field measurements around MLT ~13.3 and ~17 show a significant magnetic field depletion within the source region of EMIC waves (Figure 4, top panel; for MLT ~17, depletion is seen also in the gyrofrequency profile of the bottom panel).

2.2. Second Event: Whistler-Mode Wave-Driven Precipitation

The second event occurred on 12 May 2021. THEMIS C, in the solar wind ahead of the Earth's bow shock, observes the IP shock of an impinging ICME (Gopalswamy et al., 2003; Nitta et al., 2021) around 06:25 UT. Figures 5a–5d show the strong gradient of the magnetic field magnitude, a plasma density jump from 8 cm^{-3} to ~40 cm^{-3}, and an intensification of solar wind flow from ~−300 km/s to ~−450 km/s; the ion spectrum also shows conspicuous flow and thermal energy increases across the shock. Compared with the first event (S#1, Figure 2), the IP shock of the second event is much more distinct in form, with sharper gradients between upstream and downstream regions.

Prior to the IP shock's arrival to the Earth's magnetosphere, THEMIS A was inside the magnetosphere and observed hot stagnant ions (i.e., ion energy is above 1 keV and ion flow is around zero, see Figures 5e–5h). The shock impact compresses the magnetosphere and moves the magnetopause toward the Earth, such that THEMIS A momentarily appears to be located within the magnetosheath, with high density plasma flow observed onward from 06:40 UT. The spacecraft returns to the magnetosphere around 07:00 UT, the magnetopause evidently moving back out toward its pre-shock configuration. However, THEMIS A undergoes multiple apparent magnetopause crossings over the subsequent ~3 hr; such crossings are seen as plasma density increases along with alternating recurrences of hot rarefied and cold dense ion populations in the flux spectrum shown in Figure 5h. These successive magnetopause crossings are likely caused by magnetopause oscillation, driven by both IP shock impact and the arrival of subsequent trailing solar transients that compose the extent of the CME (observed by THEMIS C behind the initial IP shock) (see, e.g., Agapitov et al., 2009; Archer et al., 2019). During the entire interval of 06:00–10:00 UT, THEMIS A was between $L \sim 14$–17; thus observations of magnetopause crossings after 07:00 UT highlight the large amplitude character of the magnetopause oscillations.

Figure 1 shows that the IP shock compresses the magnetosphere (evidenced by the long interval of increased, positive Sym-H for S#2) and drives a substorm with AE ~−700 nT (both GOES-16 and 17 observe strong plasma sheet injections at 06:40 UT on the nightside; not shown). Additionally, after 11:00 UT there are prolonged storm activities with Sym-H around −60 nT (expected for CME impact; see Koehn et al. (2022), Tsurutani et al. (2003), and references therein), similar to what we observe for the first event, albeit more intense here. Focusing on the initial compressing shock impact at 07:00 UT, we see ELFIN B crossing the dawn-flank magnetosphere when it observes a very intense burst of electron precipitation. Figure 6 shows ELFIN detecting the relativistic electron precipitation burst around $L \sim 5.7$, with an upper energy of ~800 keV and the precipitating-to-trapped flux ratio reaching 1 for approximately the entire energy range. This burst is localized between the plasma sheet (distinguished by the absence of trapped fluxes >300 keV and the presence of isotropic fluxes <300 keV for electrons observed before 06:55 UT) and the plasmapause (recognized by the disappearance of ~300 keV fluxes after 06:56 UT; see discussions of this feature in ELFIN observations by Angelopoulos et al. (2023) and Mourenas et al. (2021)).

Panel (c) of Figure 6 shows that the precipitating-to-trapped flux ratio reaches the strong diffusion limit (~1) starting with 50 keV and remains as large as 1 up to 800 keV. Accordingly, the pitch-angle diffusion rate, $D_{\alpha\alpha}$, of the corresponding scattering mechanism should be sufficiently large for the 50 – 800 keV range. Although there have been observations of EMIC-driven precipitation of sub-relativistic electrons (Capannolo, Li, Ma, Chen, et al., 2019; Capannolo, Li, Ma, Shen, et al., 2019; Hendry et al., 2017, 2019), the efficiency of such scattering is low and the precipitating-to-trapped flux ratio tends to be much smaller than 1 (see An et al., 2022; Angelopoulos et al., 2023). In contrast, a whistler-mode resonant scattering mechanism aligns well with the character of the strong precipitation of 50–800 keV electrons observed in S#2, as the whistler-mode $D_{\alpha\alpha}$ maximizes below 100 keV (Albert, 2005; Glauert & Horne, 2005; Summers et al., 2007b) where the electron diffusion can often reach the strong diffusion limit. Previously published ELFIN observations of electron precipitations in conjunction with near-equatorial whistler-mode wave observations (see, e.g., L. Chen et al., 2022; Tsai et al., 2022) demonstrate the same precipitation pattern as the one seen in Figure 6. Considering these features in totality, we interpret this instance of relativistic electron precipitation, localized within the outer radiation belt, as an equatorial intensification of whistler-mode waves due to IP shock-induced magnetospheric compression (see, e.g., Jin et al., 2022; Yue et al., 2017). Interestingly, for this precipitation burst the strong diffusion limit is observed up to relativistic energies. Although such a strong precipitation burst resembles a microburst precipitation occurrence, Figure 6 shows that event S#2 covers two ELFIN spins (~6 s), that is, it lasts much longer than a microburst precipitation event (e.g., O'Brien et al., 2004; Shumko et al., 2021). In the Discussion section, we consider possible mechanisms that would allow whistler-mode waves to maintain high scattering efficiency up to 800 keV.

While there are no near-equatorial spacecraft observations in the dawn flank during ELFIN observations of electron precipitation, wave instruments (Kasahara et al., 2018) onboard the Arase satellite (Miyoshi et al., 2018) do detect a sharp increase of whistler-mode wave intensity (lower band chorus emission within $1-2$ kHz range and with a peak intensity of ~100 pT^2/Hz) on the nightside (MLT ~ 23) around 06:50 UT (not shown). Such wave generation is characteristic of a typical response of the magnetosphere to IP shock impact, as magnetospheric compression results in adiabatic electron heating and substorm-related electron injections from the plasma sheet. Both of these <10 keV electron populations are unstable to whistler-mode wave generation (Jin et al., 2022; Yue et al., 2017). ELFIN observations of whistler-mode wave-driven electron precipitation immediately after the shock wave arrives (as observed by THEMIS A, see Figure 5) suggest that substorm injections are unlikely to be

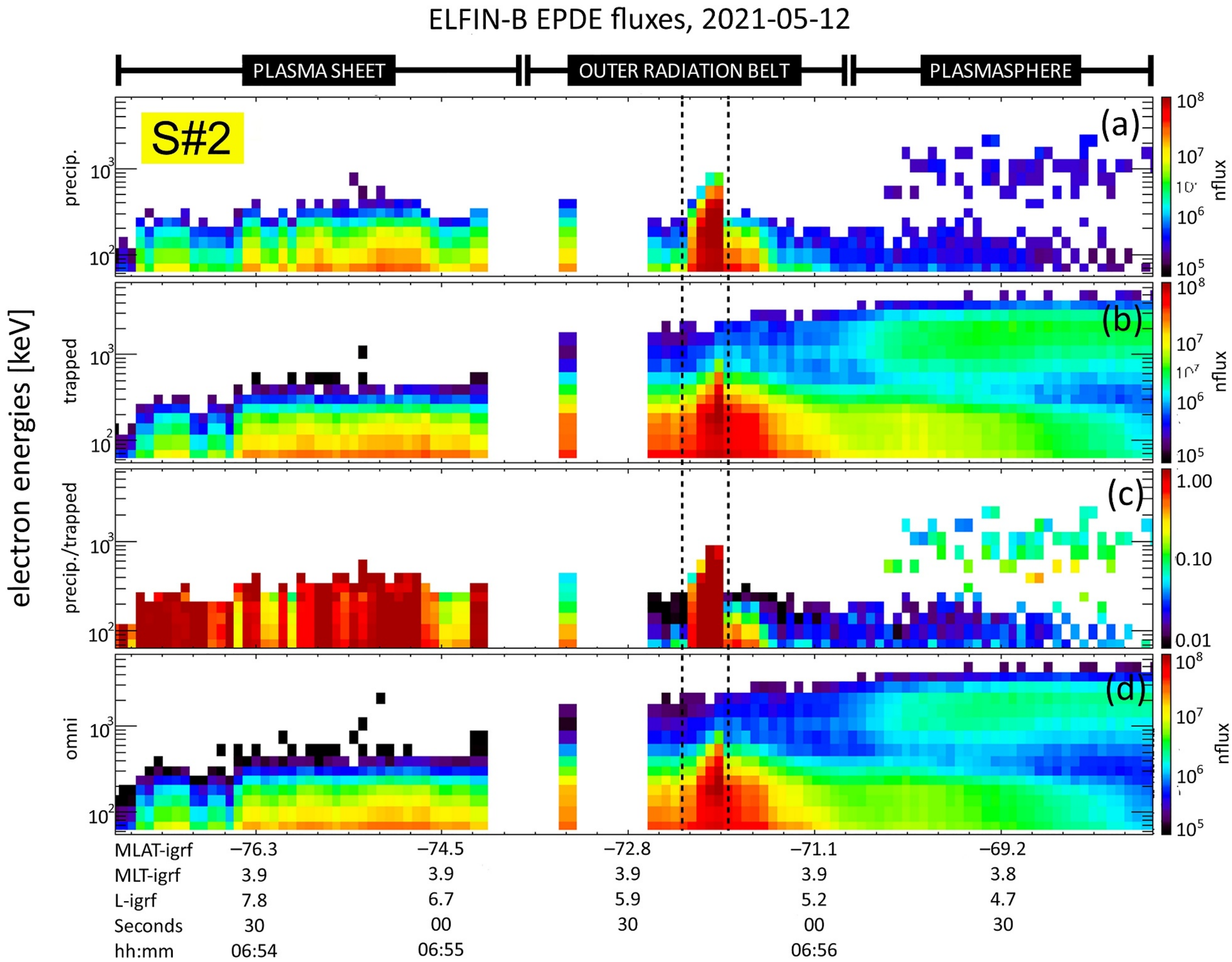

Figure 6. Overview of Electron Losses and Fields Investigation observations for event S#2 on 12 May 2021: (a) precipitating electron fluxes, (b) trapped fluxes, (c) precipitating-to-trapped flux ratios, and (d) omnidirectional fluxes. In panels (a), (b), and (d) the colorbar shows flux in [cm^{-2} s^{-1} sr^{-1} MeV^{-1}]. The dashed lines demarcate the time interval in which electron precipitation is primarily observed, as indicated in the enhancement of the precipitating-to-trapped ratio (i.e., ratio approaches unity).

the cause of wave generation for this event; the time interval between these observations is insufficient to account for electron transport inward and subsequent dawnward drift. Thus, electron adiabatic heating is the most likely scenario for the generation of whistler-mode waves.

3. Discussion

We have presented two different events with EMIC and whistler-mode wave-driven electron precipitation bursts (first event, S#1, and second event, S#2, respectively). Both events are characterized by strong solar wind drivers that either provide ion injections, followed by EMIC wave generation, or electron compressional heating, followed by whistler-mode wave generation. We now estimate the physical characteristics of EMIC and whistler-mode waves that would be required to obtain the types of electron precipitation spectra we observed for each event. We analyze two main aspects of wave generation: the resonance conditions and the cold plasma dispersion relation. First, we look at these aspects for whistler-mode waves. The most intense whistler-mode waves propagate along magnetic field lines (Agapitov et al., 2013; W. Li et al., 2011), and in cold dense plasma their dispersion relation takes the following form (Stix, 1962):

$$\omega = \Omega_{ce}(\lambda) \cdot \left(1 + \frac{\Omega_{pe}^2(\lambda)}{k^2(\lambda)c^2}\right) \quad (1)$$

or

$$k(\lambda) = \frac{\Omega_{pe}(\lambda)}{c} \cdot \left(\frac{\Omega_{ce}(\lambda)}{\omega} - 1\right)^{-1/2}$$

where the dispersion relation sets the wave number $k(\lambda)$ for a fixed wave frequency, ω. The electron gyrofrequency $\Omega_{ce} = \Omega_{ce,eq}\sqrt{1 + 3\sin^2\lambda}/\cos^6\lambda$ is given by the dipole magnetic field model ($\Omega_{ce,eq}$ is the equatorial gyrofrequency; λ is the magnetic latitude), and the plasma frequency $\Omega_{pe} = \Omega_{pe,eq}\cos^{-5/2}\lambda$ is given by the Denton et al. (2006) model ($\Omega_{pe,eq}$ is the equatorial plasma frequency; the ratio $\Omega_{pe,eq}/\Omega_{ce,eq}$ is taken from the model presented in Sheeley et al. (2001)). The resonance condition for field-aligned whistler-mode waves is:

$$\gamma\omega - k(\lambda)p_{\parallel}(\lambda)/m_e = \Omega_{ce}(\lambda) \tag{2}$$

where electron parallel momentum $p_{\parallel}$ can be written as a function of electron energy $m_e c^2(\gamma - 1)$ and equatorial pitch-angle α_{eq}:

$$p_{\parallel} = -m_e c\sqrt{\gamma^2 - 1}\sqrt{1 - \sin^2\alpha_{eq}\frac{\Omega_{ce}(\lambda)}{\Omega_{ce,eq}}} \tag{3}$$

We are interested in electron precipitation, and thus the equatorial pitch-angle should be defined by the loss cone size, $\alpha_{LC} \approx L^{-3/2} \cdot (4 - 3/L)^{-1/4}$, where L (L-shell) is defined by the radial distance (in Earth radii) of the equatorial crossing of Earth's magnetic field lines (Schulz & Lanzerotti, 1974). Combining the resonance condition 2, dispersion relation 1, and equation for $\alpha_{eq} = \alpha_{LC}$, we obtain the precipitating electron energy as a function of magnetic latitude for a given $\Omega_{pe,eq}/\Omega_{ce,eq}$.

Turning next to EMIC wave generation, the dispersion relation of field-aligned EMIC waves is (Stix, 1962)

$$\frac{k^2c^2}{\omega^2} \approx 1 - \frac{\Omega_{pe}^2}{\omega\Omega_{ce}} - \frac{\Omega_{pe}^2}{\omega}\frac{m_e}{m_p}\left(\frac{\eta_H}{\omega - \Omega_{cp}} + \frac{\eta_{He}}{\omega - \Omega_{cp}/4} + \frac{\eta_O}{\omega - \Omega_{cp}/16}\right) \tag{4}$$

where η_H, η_{He}, η_O are the relative concentrations of protons, helium ions, and oxygen ions, respectively (with $\eta_H + \eta_{He} + \eta_O = 1$), and $\Omega_{cp} = \Omega_{ce}m_e/m_p$ is the proton gyrofrequency (m_e and m_p are the electron and proton mass, respectively). For a purely proton-electron plasma, Equation 4 can be rewritten as:

$$\omega = \Omega_{cp}(\lambda) \cdot \left(\frac{k(\lambda)c}{\Omega_{pp}(\lambda)}\right)^2 \cdot \left(-\frac{1}{2} + \sqrt{\frac{1}{4} + \left(\frac{\Omega_{pp}(\lambda)}{k(\lambda)c}\right)^2}\right) \tag{5}$$

or

$$k(\lambda) = \frac{\omega}{c}\sqrt{1 + \frac{\Omega_{pp}^2(\lambda)}{\Omega_{cp}(\lambda) \cdot (\Omega_{cp}(\lambda) - \omega)}} \approx \frac{\omega}{c}\frac{\Omega_{pe}(\lambda)}{\Omega_{ce}(\lambda)}\sqrt{\frac{m_p}{m_e}}\left(1 - \frac{\omega}{\Omega_{cp}(\lambda)}\right)^{-1/2}$$

where $\Omega_{pp}^2 = \Omega_{pe}^2 m_e/m_p$. The resonance condition of Equation 2 can be rewritten for EMIC waves as

$$\gamma\omega - k(\lambda)p_{\parallel}(\lambda)/m_e = -\Omega_{ce}(\lambda) \tag{6}$$

Using these relations, we obtain resonance energies as a function of magnetic latitude and wave frequency, as displayed in Figure 7. For EMIC wave calculations we set $\Omega_{pe,eq}/\Omega_{ce,eq} = 15$ (typical for an EMIC wave generation region within the dusk flank and outside the plasmasphere, see Zhang et al., 2016), while for whistler-mode wave calculations we set $\Omega_{pe,eq}/\Omega_{ce,eq} = 5$ (typical for a whistler-mode wave generation region within the dawn flank, see Agapitov et al., 2019; Glauert & Horne, 2005). Calculations for EMIC waves (left

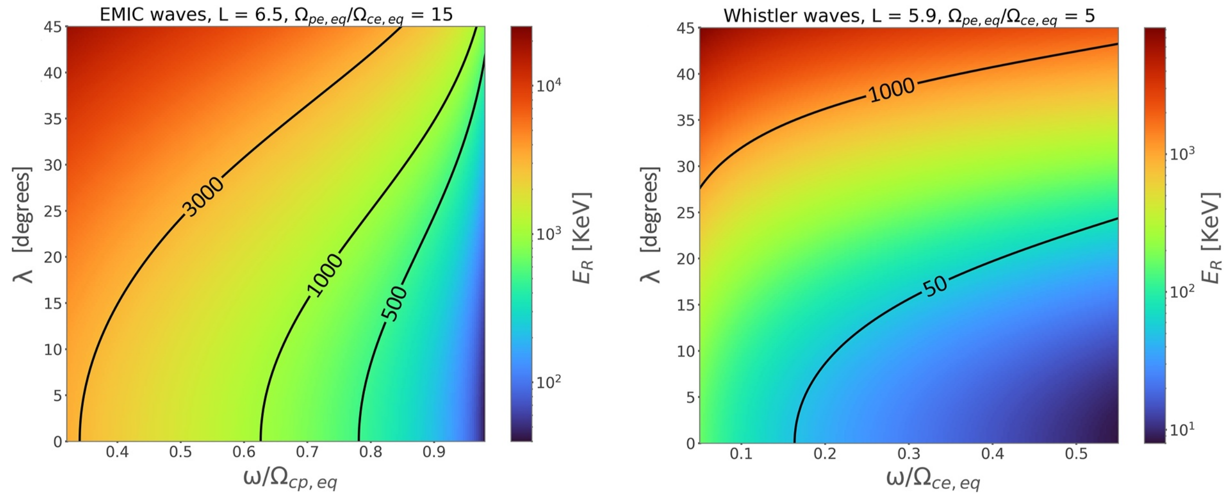

Figure 7. Resonance energy as a function of magnetic latitude λ and wave frequency ω for electromagnetic ion cyclotron waves (left panel) and whistler-mode waves (right panel). The parameters for calculation are shown at the top of each panel. Black lines represent contours of constant energy that approximately coincide with upper and lower bounds of Electron Losses and Fields Investigation precipitation observations.

panel) show that to provide precipitation of both sub-relativistic (<500 keV) and accompanying relativistic (≥1 MeV) electrons, as observed by ELFIN in S#1, the waves would likely need to be at a very high-frequency, with $\omega/\Omega_{cp,eq} > 0.8$ (see also Bashir et al., 2022; Denton et al., 2019; Ukhorskiy et al., 2010). Such a high-frequency portion of EMIC wave spectra is indeed observed around the equator (see, e.g., Zhang et al., 2016) and may provide the necessary precipitating-to-trapped flux ratio to induce the sub-relativistic precipitation associated with EMIC wave-driven relativistic electron precipitation (see Angelopoulos et al., 2023; Capannolo, Li, Ma, Chen, et al., 2019; Capannolo, Li, Ma, Shen, et al., 2019). However, at this high frequency range hot plasma effects start playing an important role in EMIC dispersion (e.g., Silin et al., 2011), and these effects generally increase the minimum resonant energy (e.g., Cao et al., 2017; L. Chen et al., 2019). For moderate wave frequencies, three additional factors could facilitate sub-relativistic precipitation by EMIC waves: (a) enhanced plasma density with $\Omega_{pe,eq}/\Omega_{ce,eq}$ exceeding the nominal (model) values (Summers & Thorne, 2003; Summers et al., 2007b), (b) non-resonant electron scattering occurring below the minimum resonance energy (effective for short EMIC wavepackets, see An et al., 2022; Chen et al., 2016; Grach & Demekhov, 2023), and/or (c) nonlinear resonant effects reducing the energy of wave-particle interactions (see discussion in Hanzelka et al. (2023) and Hendry et al. (2019)). These factors may contribute to the precipitating electron spectra that demonstrate a weak (precipitating-to-trapped ratio of ∼0.1) but finite precipitation down to 50 keV, as is seen in the first event. While sub-relativistic electron precipitation by EMIC waves have been reported in multiple other studies (e.g., Capannolo, Li, Ma, Chen, et al., 2019; Capannolo, Li, Ma, Shen, et al., 2019; Hendry et al., 2017, 2019), theoretical investigation is ongoing (see discussion in An et al. (2022), Angelopoulos et al. (2023), Denton et al. (2019), Grach and Demekhov (2023), Hanzelka et al. (2023), and Hendry et al. (2019, 2021)). The observations provided here (Figure 3) thus provide an additional instance of EMIC wave contribution to sub-relativistic electron losses, important for further theoretical study.

Concerning whistler-mode waves, the precipitation of relativistic electrons suggests a large local Ω_{ce}/Ω_{pe} (Summers et al., 2007a), indicating that such waves should propagate up to high latitudes. This is indeed the case for the second event, as the precipitating-to-trapped electron flux ratio is approximately one (i.e., at the strong diffusion limit, see Kennel, 1969) for energies up to 0.9 MeV (Figure 7, right panel shows that resonant latitudes are ∼40° for such energies and typical wave frequency $\omega/\Omega_{ce,eq} \sim 0.3$ (Agapitov et al., 2018; W. Li et al., 2011). Empirical wave intensity models, such as those of Agapitov et al. (2018) and Wang and Shprits (2019), predict that wave intensity should decrease with increasing magnetic latitude (i.e., farther away from the equator). This possible wave damping (likely due to Landau resonance with suprathermal electrons; see Bell et al., 2002; Bortnik et al., 2007; L. Chen et al., 2013) prevents effective scattering of relativistic electrons. Thus, two possible scenarios can explain the observed electron precipitation of the second event. The first scenario assumes that electrons are scattered by whistler-mode waves ducted within a small-scale density perturbation (R. Chen et al., 2021; Hosseini et al., 2021; Ke et al., 2021; Shen et al., 2021) that can trap waves and prevent their damping (see Artemyev et al., 2021; L. Chen

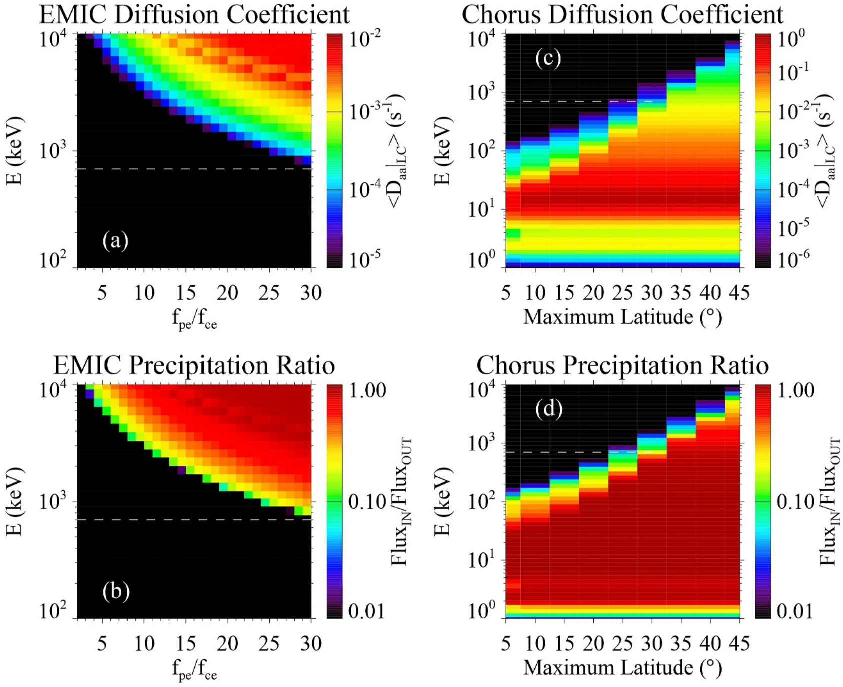

Figure 8. (a), (c) Pitch-angle diffusion rates and (b), (d) precipitating-to-trapped flux ratios for electron scattering by electromagnetic ion cyclotron (EMIC) waves and whistler-mode waves. For EMIC waves color values are shown as a function of energy and f_{pe}/f_{ce}, while for whistler-mode waves color values are shown as a function of energy and maximum wave latitude. See text for parameters used in simulations.

et al., 2022, for discussion of the wave ducting effect on electron scattering energies). The second scenario assumes that the electrons are scattered by very oblique whistler-mode waves resonating with electrons near the equator via high-order resonance: $\gamma\omega - k(\lambda)p_{\|}(\lambda)/m_e = n\Omega_{ce}(\lambda)$ with $|n| > 1$ (e.g., Artemyev et al., 2016; Lorentzen et al., 2001; Mourenas et al., 2012). Such waves can precipitate relativistic electrons even at low latitudes (see examples in Gan et al. (2023)), but require additional populations of field-aligned suprathermal electron streams to supress Landau damping and thus allow very oblique wave generation (e.g., Artemyev & Mourenas, 2020; W. Li et al., 2016; Mourenas et al., 2015; Sauer et al., 2020). Therefore, to explain the dawn-flank relativistic electron precipitation as driven by IP shock wave impact, we would need to incorporate either strong equatorial density gradients formed by convection electric fields, which could duct whistler-mode waves, or an ionospheric outflow of secondary (suprathermal, ∼100 eV) electrons (Khazanov et al., 2014, 2022) to provide the conditions for very oblique whistler-mode wave generation.

To support and extend the estimates presented in Figure 7, we perform a parametric analysis of the electron scattering rate by whistler-mode and EMIC waves (see details on utilized diffusion code in Ni et al. (2008, 2011) and Q. Ma et al. (2015)). For the first event, we use EMIC wave spectrum taken from Figure 4, averaged over the 08:00–09:00 UT interval, with the following main aspects: wave amplitude of ∼1.345 nT; lower and upper frequency cutoffs of 0.26 and 0.99 of the helium gyrofrequency; total electron density assumed to be constant along the field line; wave latitude range spanning from the equator to the latitude of crossover frequency; and plasma content of 90%:5%:5% for protons, helium ions, and oxygen ions (we use a fairly conservative estimate of heavy ion density, see Kersten et al., 2014; Ross et al., 2022). Figures 8a and 8b show pitch-angle diffusion rates at the loss cone and precipitating-to-trapped flux ratios, respectively, as a function of energy and f_{pe}/f_{ce} for these EMIC-wave settings. The simulation results confirm the resonant energy estimates: sub-MeV resonant electron scattering requires very high f_{pe}/f_{ce} (sub-relativistic scattering is likely nonresonant and cannot be described by calculated diffusion rates). We additionally verified that increasing the heavy ion density (70%:20%:10%) can reduce the resonant (precipitating) electron energy to 300 keV for $f_{pe}/f_{ce} = 30$, but this combination of high heavy ion density and large f_{pe}/f_{ce} is not typical for EMIC wave observations (see discussion in Ross et al. (2022)).

We perform a similar analysis for the second event, employing the following parameters: plasma density of 10 cm^{-3}, with density assumed to be constant along the field line (based on THEMIS A observations of plasma density in the dawn sector, after the spacecraft has returned to the magnetosphere around 10:00 UT); wave spectrum consistent with Arase measurements of night-side whistler-mode waves; and wave normal angle distribution corresponding to predominantly field-aligned waves, with a mean wave normal angle of zero and a distribution spread of 30°. Figures 8c and 8d show the resultant pitch-angle diffusion rates at the loss cone and precipitating-to-trapped flux ratios, respectively, as a function of energy and maximum magnetic latitude (for a finite wave power) for these whistler-mode wave settings. Again, simulation results confirm the resonant energy estimates: to scatter relativistic (∼1 MeV) electrons waves should propagate to $30 - 40°$ magnetic latitude (see further discussion in Artemyev et al. (2024)).

Both events of electron precipitation are characterized by relativistic electron energies (>500 keV). Electrons of such energies can penetrate to the low-altitude ionosphere, below 80 km, and significantly impact the altitude-dependent ionization profile (Pettit et al., 2023; Turunen et al., 2016). There have been multiple observations evidencing that energetic electron precipitation affects ionospheric characteristics; the most recent results were obtained for events with conjugate wave measurements from near-equatorial spacecraft, with such measurements used in combination with incoherent scatter radar measurements (e.g., Q. Ma et al., 2022; Miyoshi et al., 2021; Sanchez et al., 2022) and models of ionization as induced by precipitating particles (Fang et al., 2008; Xu et al., 2020). Therefore, the relativistic electron precipitation events presented in this study exemplify a direct connection between the dynamic character of the low ionosphere and the impacts of solar wind transient structures on the Earth's magnetosphere, as the near-equatorial generation of whistler-mode and EMIC waves and resultant wave-particle interactions provide an energy transfer mechanism between the solar wind and ionosphere.

4. Summary

In this study we explore the chain of events leading to sub-relativistic and relativistic electron precipitation during two different cases when comprehensive observations were available from the solar wind, the magnetosphere, and the ionosphere. The two events are each characterized by strong solar wind drivers that impact and compress the magnetosphere, triggering intense geomagnetic activity and electromagnetic wave intensification and ultimately culminating in distinct forms of electron precipitation. Through the combined multi-point observations of ARTEMIS, THEMIS, and the geosynchronous, low-altitude ELFIN satellites, we synthesize an explanatory model of the sequence of events that lead to the observed characteristics of precipitation. Although the effects of EMIC and whistler-mode wave activity enhancements due to solar wind transient impacts have been well explored in various previous studies (Blum et al., 2021; Jin et al., 2022; Y.-X. Li et al., 2022; Xue et al., 2022; Yan et al., 2023; Yue et al., 2017; Zuxiang et al., 2023), the two events in this paper arguably represent the first direct observations of relativistic electron losses as induced by solar wind-driven waves.

In the first event, a CIR, containing an IP shock and multiple rotational discontinuities of the solar wind, compresses the magnetosphere and drives a prolonged moderate storm with multiple substorm injections. Such injections are known to be responsible for hot ion transport into the inner magnetosphere, where the injected ion population consequently drives EMIC wave generation. We have presented low-altitude observations of resultant EMIC wave-driven losses (precipitating-to-trapped flux ratio reaches one) of sub-relativistic and relativistic electrons, spanning energies of 300 keV to ∼2 MeV within a wide latitudinal (L-shell) range. In the second event an IP coronal mass ejection, with a strong preceding IP shock, impacts and significantly compresses the magnetosphere ($Sym - H$ reaches 40 nT). Such compression is known to drive whistler-mode waves, and we have presented low-altitude observations of intense whistler wave-driven electron precipitation, encompassing a wide energy range (from 50 to 700 keV) but very localized span of latitudes (L-shells). We have examined resonance conditions and cold plasma dispersion relations in order to evaluate the expected characteristics of waves capable of producing each unique precipitation event. Using these calculations, we have discussed plausible physical factors and scenarios which could foster the proper conditions for the latitudinal distribution of these waves.

This study was largely built around ELFIN's low-altitude measurements of electron precipitation, and further investigations would benefit from the incorporation of additional near-equatorial spacecraft observations which could directly identify specific wave modes and their drivers (e.g., anisotropic ion and electron populations).

Moreover, a combination of global magnetohydrodynamic and test-particle simulations, outside the scope of this study, would be needed to verify solar wind structure impact as the main trigger for electron precipitation (see discussion in Chan et al. (2023) and Ukhorskiy et al. (2022)). The application of such models is left for future work. It should be noted that our study makes no attempt to provide any general conclusions on the difference between CIR and CME impacts and the respective global magnetospheric responses that follow. Rather, we focus on two events for which comprehensive spacecraft observations were available (the concurrence of ELFIN measurements with CME/CIR magnetospheric impacts is quite rare) to exemplify and evaluate those responses which were observed. Our study demonstrates that such solar wind impacts can lead to related phenomena in various regions of the magnetosphere, including relativistic electron precipitation at the ionosphere, and evaluates these phenomena and their mutual relation with the composite multipoint observations relevant to each event. The differing electron precipitation patterns (i.e., EMIC vs. whistler-mode wave drivers) we observe for the two events in our study are unlikely to be the direct result of the different solar wind impact types, but rather may be attributed to the different, limited MLT domains that ELFIN observations cover for each event. Future investigations, supplemented with the observations of upcoming CubeSat missions (e.g., X. Li et al., 2024; Millan et al., 2022), may benefit from more observational conjunctions of large-scale solar wind transient impacts with electron precipitation events, allowing for more comprehensive assessment of CME and CIR influence in the driving of electron precipitation globally.

Data Availability Statement

ELFIN data is available at ELFIN (2024). THEMIS&ARTEMIS data is available at THEMIS (2024). Sym-H and AE indexes were downloaded from SUPERMAG (2024). GEO-KOMPSAT-2A (SOSMAG) data is made available via ESA's Space Safety Programme and its provision forms part of the ESA Space Weather Service System at SOSMAG (2024). Data access and processing was done using SPEDAS V3.1, see Angelopoulos et al. (2019).

Acknowledgments
We acknowledge support from NASA contract NAS5-02099. Work at Los Alamos National Laboratory was performed under the auspices of the United States Department of Energy. Q.M. would like to acknowledge the NASA Grant 80NSSC20K0196 and NSF grant AGS-2225445. A.V.A and X.-J.Z. acknowledge support from the NASA Grants 80NSSC23K0108, 80NSSC23K0403, 80NSSC24K0138, 80NSSC20K0689, and from the NSF Grant 2021749. V.A. and A. R. also acknowledge support from NSF Grants AGS-1242918, AGS-2019950. We are grateful to NASA's CubeSat Launch Initiative for ELFIN's successful launch. We acknowledge early support of the ELFIN project by the AFOSR, under its University Nanosat Program; by the UNP-8 project, contract FA9453-12-D-0285; and by the California Space Grant program. We acknowledge the critical contributions of the numerous volunteer ELFIN team student members. We acknowledge the GEO-KOMPSAT-2A magnetometer team (Ulrich Auster, Dragos Constantinescu; Institut für Geophysik und Extraterrestrische Physik, Technische Universität Braunschweig, Braunschweig, Germany) for their high quality data set. We also acknowledge the support of NASA contract NAS5-02099 for the use of data from the THEMIS Mission, specifically K. H.Glassmeier, U. Auster, and W. Baumjohann for the use of FGM data (provided under the lead of the Technical University of Braunschweig and with financial support through the German Ministry for Economy and Technology and the German Center for Aviation and Space (DLR) under contract 50 OC 0302) and C. W. Carlson, J. P. McFadden for the use of ESA data.

References

Agapitov, O. V., Artemyev, A., Krasnoselskikh, V., Khotyaintsev, Y. V., Mourenas, D., Breuillard, H., et al. (2013). Statistics of whistler mode waves in the outer radiation belt: Cluster STAFF-SA measurements. *Journal of Geophysical Research*, *118*(6), 3407–3420. https://doi.org/10.1002/jgra.50312

Agapitov, O. V., Glassmeier, K.-H., Plaschke, F., Auster, H.-U., Constantinescu, D., Angelopoulos, V., et al. (2009). Surface waves and field line resonances: A THEMIS case study. *Journal of Geophysical Research*, *114*(A1), A00C27. https://doi.org/10.1029/2008JA013553

Agapitov, O. V., Mourenas, D., Artemyev, A., Hospodarsky, G., & Bonnell, J. W. (2019). Time scales for electron quasi-linear diffusion by lower-band chorus waves: The effects of ω_{pe}/Ω_{ce} dependence on geomagnetic activity. *Geophysical Research Letters*, *46*(12), 6178–6187. https://doi.org/10.1029/2019GL083446

Agapitov, O. V., Mourenas, D., Artemyev, A. V., Mozer, F. S., Hospodarsky, G., Bonnell, J., & Krasnoselskikh, V. (2018). Synthetic empirical chorus wave model from combined Van Allen probes and cluster statistics. *Journal of Geophysical Research: Space Physics*, *123*(1), 297–314. https://doi.org/10.1002/2017JA024843

Albert, J. M. (2005). Evaluation of quasi-linear diffusion coefficients for whistler mode waves in a plasma with arbitrary density ratio. *Journal of Geophysical Research*, *110*(A3), 3218. https://doi.org/10.1029/2004JA010844

Alves, M. V., Echer, E., & Gonzalez, W. D. (2006). Geoeffectiveness of corotating interaction regions as measured by Dst index. *Journal of Geophysical Research: Space Physics*, *111*(A7), A07S05. https://doi.org/10.1029/2005JA011379

An, X., Artemyev, A., Angelopoulos, V., Zhang, X., Mourenas, D., & Bortnik, J. (2022). Nonresonant scattering of relativistic electrons by electromagnetic ion cyclotron waves in Earth's radiation belts. *Physical Review Letters*, *129*(13), 135101. https://doi.org/10.1103/PhysRevLett.129.135101

Angelopoulos, V. (2008). The THEMIS mission. *Space Science Reviews*, *141*(1–4), 5–34. https://doi.org/10.1007/s11214-008-9336-1

Angelopoulos, V., Cruce, P., Drozdov, A., Grimes, E. W., Hatzigeorgiu, N., King, D. A., et al. (2019). The space physics environment data analysis system (SPEDAS). *Space Science Reviews*, *215*(1), 9. https://doi.org/10.1007/s11214-018-0576-4

Angelopoulos, V., Tsai, E., Bingley, L., Shaffer, C., Turner, D. L., Runov, A., et al. (2020). The ELFIN mission. *Space Science Reviews*, *216*(5), 103. https://doi.org/10.1007/s11214-020-00721-7

Angelopoulos, V., Zhang, X. J., Artemyev, A. V., Mourenas, D., Tsai, E., Wilkins, C., et al. (2023). Energetic electron precipitation driven by electromagnetic ion cyclotron waves from ELFIN's low altitude perspective. *Space Science Reviews*, *219*(5), 37. https://doi.org/10.1007/s11214-023-00984-w

Archer, M. O., Hietala, H., Hartinger, M. D., Plaschke, F., & Angelopoulos, V. (2019). Direct observations of a surface eigenmode of the dayside magnetopause. *Nature Communications*, *10*(1), 615. https://doi.org/10.1038/s41467-018-08134-5

Artemyev, A. V., Agapitov, O., Mourenas, D., Krasnoselskikh, V., Shastun, V., & Mozer, F. (2016). Oblique whistler-mode waves in the Earth's inner magnetosphere: Energy distribution, origins, and role in radiation belt dynamics. *Space Science Reviews*, *200*(1–4), 261–355. https://doi.org/10.1007/s11214-016-0252-5

Artemyev, A. V., Angelopoulos, V., & McTiernan, J. M. (2018). Near-Earth solar wind: Plasma characteristics from ARTEMIS measurements. *Journal of Geophysical Research: Space Physics*, *123*(12), 9955–9962. https://doi.org/10.1029/2018JA025904

Artemyev, A. V., Angelopoulos, V., Zhang, X. J., Runov, A., Petrukovich, A., Nakamura, R., et al. (2022). Thinning of the magnetotail current sheet inferred from low-altitude observations of energetic electrons. *Journal of Geophysical Research: Space Physics*, *127*(10), e2022JA030705. https://doi.org/10.1029/2022JA030705

Artemyev, A. V., Demekhov, A. G., Zhang, X. J., Angelopoulos, V., Mourenas, D., Fedorenko, Y. V., et al. (2021). Role of ducting in relativistic electron loss by whistler-mode wave scattering. *Journal of Geophysical Research: Space Physics*, *126*(11), e29851. https://doi.org/10.1029/2021JA029851

Artemyev, A. V., & Mourenas, D. (2020). On whistler mode wave relation to electron field-aligned plateau populations. *Journal of Geophysical Research: Space Physics*, *125*(3), e27735. https://doi.org/10.1029/2019JA027735

Artemyev, A. V., Zhang, X. J., Demekhov, A. G., Meng, X., Angelopoulos, V., & Fedorenko, Y. V. (2024). Relativistic electron precipitation driven by mesoscale transients, inferred from ground and multi-spacecraft platforms. *Journal of Geophysical Research: Space Physics*, *129*(2), e2023JA032287. https://doi.org/10.1029/2023JA032287

Auster, H. U., Glassmeier, K. H., Magnes, W., Aydogar, O., Baumjohann, W., Constantinescu, D., et al. (2008). The THEMIS fluxgate magnetometer. *Space Science Reviews*, *141*(1–4), 235–264. https://doi.org/10.1007/s11214-008-9365-9

Bashir, M. F., Artemyev, A., Zhang, X.-J., & Angelopoulos, V. (2022). Hot plasma effects on electron resonant scattering by electromagnetic ion cyclotron waves. *Geophysical Research Letters*, *49*(11), e99229. https://doi.org/10.1029/2022GL099229

Bell, T. F., Inan, U. S., Bortnik, J., & Scudder, J. D. (2002). The Landau damping of magnetospherically reflected whistlers within the plasmasphere. *Geophysical Research Letters*, *29*(15), 1733. https://doi.org/10.1029/2002GL014752

Bezděková, B., Němec, F., Parrot, M., Kruparova, O., & Krupar, V. (2021). Using principal component analysis to characterize the variability of VLF wave intensities measured by a low altitude spacecraft and caused by interplanetary shocks. *Journal of Geophysical Research: Space Physics*, *126*(5), e29158. https://doi.org/10.1029/2021JA029158

Birn, J., Runov, A., & Hesse, M. (2015). Energetic ions in dipolarization events. *Journal of Geophysical Research*, *120*(9), 7698–7717. https://doi.org/10.1002/2015JA021372

Blake, J. B., Baker, D. N., Turner, N., Ogilvie, K. W., & Lepping, R. P. (1997). Correlation of changes in the outer-zone relativistic-electron population with upstream solar wind and magnetic field measurements. *Geophysical Research Letters*, *24*(8), 927–929. https://doi.org/10.1029/97GL00859

Blum, L. W., Agapitov, O., Bonnell, J. W., Kletzing, C., & Wygant, J. (2016). EMIC wave spatial and coherence scales as determined from multipoint Van Allen Probe measurements. *Geophysical Research Letters*, *43*(10), 4799–4807. https://doi.org/10.1002/2016GL068799

Blum, L. W., Bonnell, J. W., Agapitov, O., Paulson, K., & Kletzing, C. (2017). EMIC wave scale size in the inner magnetosphere: Observations from the dual Van Allen Probes. *Geophysical Research Letters*, *44*(3), 1227–1233. https://doi.org/10.1002/2016GL072316

Blum, L. W., Koval, A., Richardson, I. G., Wilson, L. B., Malaspina, D., Greeley, A., & Jaynes, A. N. (2021). Prompt response of the dayside magnetosphere to discrete structures within the sheath region of a coronal mass ejection. *Geophysical Research Letters*, *48*(11), e92700. https://doi.org/10.1029/2021GL092700

Blum, L. W., Remya, B., Denton, M. H., & Schiller, Q. (2020). Persistent EMIC wave activity across the nightside inner magnetosphere. *Geophysical Research Letters*, *47*(6), e87009. https://doi.org/10.1029/2020GL087009

Bortnik, J., Thorne, R. M., Meredith, N. P., & Santolik, O. (2007). Ray tracing of penetrating chorus and its implications for the radiation belts. *Geophysical Research Letters*, *34*(15), L15109. https://doi.org/10.1029/2007GL030040

Boudouridis, A., Rodriguez, J. V., Kress, B. T., Dichter, B. K., & Onsager, T. G. (2020). Development of a bowtie inversion technique for real-time processing of the GOES-16/-17 SEISS MPS-HI electron channels. *Space Weather*, *18*(4), e02403. https://doi.org/10.1029/2019SW002403

Breneman, A. W., Halford, A. J., Millan, R. M., Woodger, L. A., Zhang, X. J., Sandhu, J. K., et al. (2020). Driving of outer belt electron loss by solar wind dynamic pressure structures: Analysis of balloon and satellite data. *Journal of Geophysical Research: Space Physics*, *125*(12), e28097. https://doi.org/10.1029/2020JA028097

Burch, J. L., Torbert, R. B., Phan, T. D., Chen, L.-J., Moore, T. E., Ergun, R. E., et al. (2016). Electron-scale measurements of magnetic reconnection in space. *Science*, *352*(6290). https://doi.org/10.1126/science.aaf2939

Cao, J., Shprits, Y. Y., Ni, B., & Zhelavskaya, I. S. (2017). Scattering of ultra-relativistic electrons in the Van Allen radiation belts accounting for hot plasma effects. *Scientific Reports*, *7*(1), 17719. https://doi.org/10.1038/s41598-017-17739-7

Capannolo, L., Li, W., Ma, Q., Chen, L., Shen, X. C., Spence, H. E., et al. (2019). Direct observation of subrelativistic electron precipitation potentially driven by EMIC waves. *Geophysical Research Letters*, *46*(22), 12711–12721. https://doi.org/10.1029/2019GL084202

Capannolo, L., Li, W., Ma, Q., Qin, M., Shen, X. C., Angelopoulos, V., et al. (2023). Electron precipitation observed by ELFIN using proton precipitation as a proxy for electromagnetic ion cyclotron (EMIC) waves. *Geophysical Research Letters*, *50*(21), e2023GL103519. https://doi.org/10.1029/2023GL103519

Capannolo, L., Li, W., Ma, Q., Shen, X.-C., Zhang, X.-J., Redmon, R. J., et al. (2019). Energetic electron precipitation: Multievent analysis of its spatial extent during emic wave activity. *Journal of Geophysical Research: Space Physics*, *124*(4), 2466–2483. https://doi.org/10.1029/2018JA026291

Chan, A. A., Elkington, S. R., Longley, W. J., Aldhurais, S. A., Alam, S. S., Albert, J. M., et al. (2023). Simulation of radiation belt wave-particle interactions in an mhd-particle framework. *Frontiers in Astronomy and Space Sciences*, *10*. https://doi.org/10.3389/fspas.2023.1239160

Chen, H., Gao, X., Lu, Q., Tsurutani, B. T., & Wang, S. (2020). Statistical evidence for EMIC wave excitation driven by substorm injection and enhanced solar wind pressure in the Earth's magnetosphere: Two different EMIC wave sources. *Geophysical Research Letters*, *47*(21), e90275. https://doi.org/10.1029/2020GL090275

Chen, L., Thorne, R. M., & Bortnik, J. (2011). The controlling effect of ion temperature on EMIC wave excitation and scattering. *Geophysical Research Letters*, *38*(16), L16109. https://doi.org/10.1029/2011GL048653

Chen, L., Thorne, R. M., Bortnik, J., & Zhang, X.-J. (2016). Nonresonant interactions of electromagnetic ion cyclotron waves with relativistic electrons. *Journal of Geophysical Research*, *121*(10), 9913–9925. https://doi.org/10.1002/2016JA022813

Chen, L., Thorne, R. M., & Horne, R. B. (2009). Simulation of EMIC wave excitation in a model magnetosphere including structured high-density plumes. *Journal of Geophysical Research: Space Physics*, *114*(A7), A07221. https://doi.org/10.1029/2009JA014204

Chen, L., Thorne, R. M., Jordanova, V. K., Wang, C.-P., Gkioulidou, M., Lyons, L., & Horne, R. B. (2010). Global simulation of EMIC wave excitation during the 21 April 2001 storm from coupled RCM-RAM-HOTRAY modeling. *Journal of Geophysical Research: Space Physics*, *115*(A7), A07209. https://doi.org/10.1029/2009JA015075

Chen, L., Thorne, R. M., Li, W., & Bortnik, J. (2013). Modeling the wave normal distribution of chorus waves. *Journal of Geophysical Research*, *118*(3), 1074–1088. https://doi.org/10.1029/2012JA018343

Chen, L., Zhang, X.-J., Artemyev, A., Angelopoulos, V., Tsai, E., Wilkins, C., & Horne, R. B. (2022). Ducted chorus waves cause sub-relativistic and relativistic electron microbursts. *Geophysical Research Letters*, *49*(5), e97559. https://doi.org/10.1029/2021GL097559

Chen, L., Zhang, X.-J., Artemyev, A., Zheng, L., Xia, Z., Breneman, A. W., & Horne, R. B. (2021). Electron microbursts induced by nonducted chorus waves. *Frontiers in Astronomy and Space Sciences*, *8*, 163. https://doi.org/10.3389/fspas.2021.745927

Chen, L., Zhu, H., & Zhang, X. (2019). Wavenumber analysis of EMIC waves. *Geophysical Research Letters*, *46*(11), 5689–5697. https://doi.org/10.1029/2019GL082686

Chen, R., Gao, X., Lu, Q., Chen, L., Tsurutani, B. T., Li, W., & Wang, S. (2021). In situ observations of whistler mode chorus waves guided by density ducts. *Journal of Geophysical Research: Space Physics*, *126*(4), e28814. https://doi.org/10.1029/2020JA028814

Constantinescu, O. D., Auster, H.-U., Delva, M., Hillenmaier, O., Magnes, W., & Plaschke, F. (2020). Principal component gradiometer technique for removal of spacecraft-generated disturbances from magnetic field data. *Geoscientific Instrumentation, Methods and Data Systems Discussions*, *25*, 1–26. https://doi.org/10.5194/gi-2020-10

Daglis, I. A., Thorne, R. M., Baumjohann, W., & Orsini, S. (1999). The terrestrial ring current: Origin, formation, and decay. *Reviews of Geophysics*, *37*(4), 407–438. https://doi.org/10.1029/1999RG900009

Da Silva, L. A., Shi, J., Marchezi, J. P., Agapitov, O. V., Sibeck, D., Alves, L. R., et al. (2023). High-energy electron flux enhancement pattern in the outer radiation belt in response to the interplanetary coronal mass ejections. *Journal of Geophysical Research: Space Physics*, *128*(11), e2023JA031360. https://doi.org/10.1029/2023JA031360

Denton, R. E., Ofman, L., Shprits, Y. Y., Bortnik, J., Millan, R. M., Rodger, C. J., et al. (2019). Pitch angle scattering of sub-MeV relativistic electrons by electromagnetic ion cyclotron waves. *Journal of Geophysical Research: Space Physics*, *124*(7), 5610–5626. https://doi.org/10.1029/2018JA026384

Denton, R. E., Takahashi, K., Galkin, I. A., Nsumei, P. A., Huang, X., Reinisch, B. W., et al. (2006). Distribution of density along magnetospheric field lines. *Journal of Geophysical Research*, *111*(A4), 4213. https://doi.org/10.1029/2005JA011414

Dichter, B. K., Galica, G. E., McGarity, J. O., Tsui, S., Golightly, M. J., Lopate, C., & Connell, J. J. (2015). Specification, design, and calibration of the space weather suite of instruments on the NOAA GOES-R program spacecraft. *IEEE Transactions on Nuclear Science*, *62*(6), 2776–2783. https://doi.org/10.1109/TNS.2015.2477997

ELFIN. (2024). Electron losses and fields investigation (ELFIN) data archive [Dataset]. https://data.elfin.ucla.edu/

Engebretson, M. J., Posch, J. L., Wygant, J. R., Kletzing, C. A., Lessard, M. R., Huang, C.-L., et al. (2015). Van Allen probes, NOAA, GOES, and ground observations of an intense EMIC wave event extending over 12 h in magnetic local time. *Journal of Geophysical Research*, *120*(7), 5465–5488. https://doi.org/10.1002/2015JA021227

Fang, X., Randall, C. E., Lummerzheim, D., Solomon, S. C., Mills, M. J., Marsh, D. R., et al. (2008). Electron impact ionization: A new parameterization for 100 eV to 1 MeV electrons. *Journal of Geophysical Research: Space Physics*, *113*(A9), A09311. https://doi.org/10.1029/2008JA013384

Gan, L., Artemyev, A., Li, W., Zhang, X.-J., Ma, Q., Mourenas, D., et al. (2023). Bursty energetic electron precipitation by high-order resonance with very-oblique whistler-mode waves. *Geophysical Research Letters*, *50*(8), e2022GL101920. https://doi.org/10.1029/2022GL101920

Gkioulidou, M., Ukhorskiy, A. Y., Mitchell, D. G., & Lanzerotti, L. J. (2016). Storm time dynamics of ring current protons: Implications for the long-term energy budget in the inner magnetosphere. *Geophysical Research Letters*, *43*(10), 4736–4744. https://doi.org/10.1002/2016GL068013

Gkioulidou, M., Ukhorskiy, A. Y., Mitchell, D. G., Sotirelis, T., Mauk, B. H., & Lanzerotti, L. J. (2014). The role of small-scale ion injections in the buildup of Earth's ring current pressure: Van Allen Probes observations of the 17 March 2013 storm. *Journal of Geophysical Research*, *119*(9), 7327–7342. https://doi.org/10.1002/2014JA020096

Glauert, S. A., & Horne, R. B. (2005). Calculation of pitch angle and energy diffusion coefficients with the PADIE code. *Journal of Geophysical Research*, *110*(A4), 4206. https://doi.org/10.1029/2004JA010851

Gonzalez, W. D., Tsurutani, B. T., & Clúa de Gonzalez, A. L. (1999). Interplanetary origin of geomagnetic storms. *Space Science Reviews*, *88*(3/4), 529–562. https://doi.org/10.1023/A:1005160129098

Gopalswamy, N., Shimojo, M., Lu, W., Yashiro, S., Shibasaki, K., & Howard, R. A. (2003). Prominence eruptions and coronal mass ejection: A statistical study using microwave observations. *The Astrophysical Journal*, *586*(1), 562–578. https://doi.org/10.1086/367614

Gosling, J. T. (1996). Corotating and transient solar wind flows in three dimensions. *Annual Review of Astronomy and Astrophysics*, *34*(1), 35–74. https://doi.org/10.1146/annurev.astro.34.1.35

Grach, V. S., Artemyev, A. V., Demekhov, A. G., Zhang, X.-J., Bortnik, J., Angelopoulos, V., et al. (2022). Relativistic electron precipitation by EMIC waves: Importance of nonlinear resonant effects. *Geophysical Research Letters*, *49*(17), e99994. https://doi.org/10.1029/2022GL099994

Grach, V. S., & Demekhov, A. G. (2023). Interaction of relativistic electrons with packets of the electromagnetic ion cyclotron waves of finite length and low amplitude. *Plasma Physics Reports*, *49*(7), 901–911. https://doi.org/10.1134/S1063780X23600561

Hajra, R., Echer, E., Tsurutani, B. T., & Gonzalez, W. D. (2014). Superposed epoch analyses of HILDCAAs and their interplanetary drivers: Solar cycle and seasonal dependences. *Journal of Atmospheric and Solar-Terrestrial Physics*, *121*, 24–31. https://doi.org/10.1016/j.jastp.2014.09.012

Hajra, R., Tsurutani, B. T., Echer, E., Gonzalez, W. D., & Santolik, O. (2015). Relativistic (e > 0.6, > 2.0, and > 4.0 MeV) Electron Acceleration at Geosynchronous Orbit during High-intensity, Long-duration, Continuous AE Activity (HILDCAA) Events. *The Astrophysical Journal*, *799*(1), 39. https://doi.org/10.1088/0004-637X/799/1/39

Hanzelka, M., Li, W., & Ma, Q. (2023). Parametric analysis of pitch angle scattering and losses of relativistic electrons by oblique EMIC waves. *Frontiers in Astronomy and Space Sciences*, *10*, 1163515. https://doi.org/10.3389/fspas.2023.1163515

Hasegawa, H., Fujimoto, M., Phan, T.-D., Rème, H., Balogh, A., Dunlop, M. W., et al. (2004). Transport of solar wind into Earth's magnetosphere through rolled-up Kelvin-Helmholtz vortices. *Nature*, *430*(7001), 755–758. https://doi.org/10.1038/nature02799

He, Z., Chen, L., Zhu, H., Xia, Z., Reeves, G. D., Xiong, Y., et al. (2017). Multiple-satellite observation of magnetic dip event during the substorm on 10 October 2013. *Geophysical Research Letters*, *44*(18), 9167–9175. https://doi.org/10.1002/2017GL074869

Heber, B., Sanderson, T. R., & Zhang, M. (1999). Corotating interaction regions. *Advances in Space Research*, *23*(3), 567–579. https://doi.org/10.1016/S0273-1177(99)80013-1

Hendry, A. T., Rodger, C. J., & Clilverd, M. A. (2017). Evidence of sub-MeV EMIC-driven electron precipitation. *Geophysical Research Letters*, *44*(3), 1210–1218. https://doi.org/10.1002/2016GL071807

Hendry, A. T., Rodger, C. J., Clilverd, M. A., & Morley, S. K. (2021). Evidence of sub MeV EMIC driven trapped electron flux dropouts from GPS observations. *Geophysical Research Letters*, *48*(9), e92664. https://doi.org/10.1029/2021GL092664

Hendry, A. T., Santolik, O., Kletzing, C. A., Rodger, C. J., Shiokawa, K., & Baishev, D. (2019). Multi-instrument observation of nonlinear EMIC-driven electron precipitation at sub-MeV energies. *Geophysical Research Letters*, *46*(13), 7248–7257. https://doi.org/10.1029/2019GL082401

Hendry, A. T., Santolik, O., Miyoshi, Y., Matsuoka, A., Rodger, C. J., Clilverd, M. A., et al. (2020). A multi-instrument approach to determining the source-region extent of EEP-driving EMIC waves. *Geophysical Research Letters*, *47*(7), e86599. https://doi.org/10.1029/2019GL086599

Hosseini, P., Agapitov, O., Harid, V., & Gołkowski, M. (2021). Evidence of small scale plasma irregularity effects on whistler mode chorus propagation. *Geophysical Research Letters*, *48*(5), e92850. https://doi.org/10.1029/2021GL092850

Jin, Y., Liu, N., Su, Z., Zheng, H., Wang, Y., & Wang, S. (2022). Immediate impact of solar wind dynamic pressure pulses on whistler-mode chorus waves in the inner magnetosphere. *Geophysical Research Letters*, *49*(5), e2022GL097941. https://doi.org/10.1029/2022GL097941
Jun, C.-W., Miyoshi, Y., Kurita, S., Yue, C., Bortnik, J., Lyons, L., et al. (2021). The characteristics of EMIC waves in the magnetosphere based on the Van Allen Probes and Arase observations. *Journal of Geophysical Research: Space Physics*, *126*(6), e29001. https://doi.org/10.1029/2020JA029001
Jun, C. W., Miyoshi, Y., Nakamura, S., Shoji, M., Hori, T., Bortnik, J., et al. (2024). A triggering process for nonlinear EMIC waves driven by the compression of the dayside magnetosphere. *Geophysical Research Letters*, *51*(1), e2023GL106860. https://doi.org/10.1029/2023GL106860
Jun, C. W., Yue, C., Bortnik, J., Lyons, L. R., Nishimura, Y., & Kletzing, C. (2019). EMIC wave properties associated with and without injections in the inner magnetosphere. *Journal of Geophysical Research: Space Physics*, *124*(3), 2029–2045. https://doi.org/10.1029/2018JA026279
Kasahara, Y., Kasaba, Y., Kojima, H., Yagitani, S., Ishisaka, K., Kumamoto, A., et al. (2018). The plasma wave experiment (PWE) on board the Arase (ERG) satellite. *Earth Planets and Space*, *70*(1), 86. https://doi.org/10.1186/s40623-018-0842-4
Ke, Y., Chen, L., Gao, X., Lu, Q., Wang, X., Chen, R., et al. (2021). Whistler mode waves trapped by density irregularities in the Earth's magnetosphere. *Geophysical Research Letters*, *48*(7), e92305. https://doi.org/10.1029/2020GL092305
Kennel, C. F. (1966). Low-frequency whistler mode. *Physics of Fluids*, *9*(11), 2190–2202. https://doi.org/10.1063/1.1761588
Kennel, C. F. (1969). Consequences of a magnetospheric plasma. *Reviews of Geophysics and Space Physics*, *7*(1–2), 379–419. https://doi.org/10.1029/RG007i001p00379
Kennel, C. F., & Petschek, H. E. (1966). Limit on stably trapped particle fluxes. *Journal of Geophysical Research*, *71*, 1–28. https://doi.org/10.1029/jz071i001p00001
Kersten, T., Horne, R. B., Glauert, S. A., Meredith, N. P., Fraser, B. J., & Grew, R. S. (2014). Electron losses from the radiation belts caused by EMIC waves. *Journal of Geophysical Research*, *119*(11), 8820–8837. https://doi.org/10.1002/2014JA020366
Khazanov, G. V., Glocer, A., & Himwich, E. W. (2014). Magnetosphere-ionosphere energy interchange in the electron diffuse aurora. *Journal of Geophysical Research: Space Physics*, *119*(1), 171–184. https://doi.org/10.1002/2013JA019325
Khazanov, G. V., Ma, Q., & Chu, M. (2022). Electron heat fluxes generated by intense whistler waves at the upper ionospheric altitudes. *Journal of Geophysical Research: Space Physics*, *127*(9), e2022JA030753. https://doi.org/10.1029/2022JA030753
King, J. H., & Papitashvili, N. E. (2005). Solar wind spatial scales in and comparisons of hourly Wind and ACE plasma and magnetic field data. *Journal of Geophysical Research*, *110*(A2), A02104. https://doi.org/10.1029/2004JA010649
Kivelson, M. G., & Russell, C. T. (1995). Introduction to space physics.
Koehn, G. J., Desai, R. T., Davies, E. E., Forsyth, R. J., Eastwood, J. P., & Poedts, S. (2022). Successive interacting coronal mass ejections: How to create a perfect storm. *The Astrophysical Journal*, *941*(2), 139. https://doi.org/10.3847/1538-4357/aca28c
Li, W., Bortnik, J., Thorne, R. M., & Angelopoulos, V. (2011). Global distribution of wave amplitudes and wave normal angles of chorus waves using THEMIS wave observations. *Journal of Geophysical Research*, *116*(A12), 12205. https://doi.org/10.1029/2011JA017035
Li, W., Mourenas, D., Artemyev, A. V., Bortnik, J., Thorne, R. M., Kletzing, C. A., et al. (2016). Unraveling the excitation mechanisms of highly oblique lower band chorus waves. *Geophysical Research Letters*, *43*(17), 8867–8875. https://doi.org/10.1002/2016GL070386
Li, W., Ni, B., Thorne, R. M., Bortnik, J., Green, J. C., Kletzing, C. A., et al. (2013). Constructing the global distribution of chorus wave intensity using measurements of electrons by the POES satellites and waves by the Van Allen Probes. *Geophysical Research Letters*, *40*(17), 4526–4532. https://doi.org/10.1002/grl.50920
Li, X., Selesnick, R., Mei, Y., O'Brien, D., Hogan, B., Xiang, Z., et al. (2024). First results from REPTile-2 measurements onboard Cirbe. *Geophysical Research Letters*, *51*(3), e2023GL107521. https://doi.org/10.1029/2023GL107521
Li, Y.-X., Yue, C., Ma, Q., Liu, J., Zong, Q.-G., Zhou, X.-Z., et al. (2022). Simultaneous cross-energy ion response and wave generation after the impact of an interplanetary shock. *Journal of Geophysical Research: Space Physics*, *127*(11), e2022JA030636. https://doi.org/10.1029/2022JA030636
Liu, N., Jin, Y., He, Z., Yu, J., Li, K., & Cui, J. (2022). Simultaneous evolutions of inner magnetospheric plasmaspheric hiss and EMIC waves under the influence of a heliospheric plasma sheet. *Geophysical Research Letters*, *49*(10), e98798. https://doi.org/10.1029/2022GL098798
Lorentzen, K. R., Blake, J. B., Inan, U. S., & Bortnik, J. (2001). Observations of relativistic electron microbursts in association with VLF chorus. *Journal of Geophysical Research*, *106*(A4), 6017–6028. https://doi.org/10.1029/2000JA003018
Lubchich, A. A., & Semenova, N. V. (2015). Modeling of the electromagnetic ion cyclotron wave generation in the H^+-He^+ plasma of the inner magnetosphere. *Journal of Atmospheric and Solar-Terrestrial Physics*, *125*, 21–37. https://doi.org/10.1016/j.jastp.2015.02.004
Lyons, L. R., Lee, D.-Y., Thorne, R. M., Horne, R. B., & Smith, A. J. (2005). Solar wind-magnetosphere coupling leading to relativistic electron energization during high-speed streams. *Journal of Geophysical Research*, *110*(A11), 11202. https://doi.org/10.1029/2005JA011254
Ma, Q., Li, W., Thorne, R. M., Ni, B., Kletzing, C. A., Kurth, W. S., et al. (2015). Modeling inward diffusion and slow decay of energetic electrons in the Earth's outer radiation belt. *Geophysical Research Letters*, *42*(4), 987–995. https://doi.org/10.1002/2014GL062977
Ma, Q., Xu, W., Sanchez, E. R., Marshall, R. A., Bortnik, J., Reyes, P. M., et al. (2022). Analysis of electron precipitation and ionospheric density enhancements due to hiss using incoherent scatter radar and Arase observations. *Journal of Geophysical Research: Space Physics*, *127*(8), e30545. https://doi.org/10.1029/2022JA030545
Ma, X. H., Zong, Q. G., Yue, C., Hao, Y. X., & Liu, Y. (2021). Energetic electron enhancement and dropout echoes induced by solar wind dynamic pressure decrease: The effect of phase space density profile. *Journal of Geophysical Research: Space Physics*, *126*(3), e28863. https://doi.org/10.1029/2020JA028863
Magnes, W., Hillenmaier, O., Auster, H. U., Brown, P., Kraft, S., Seon, J., et al. (2020). Space weather magnetometer aboard GEO-KOMPSAT-2A. *Space Science Reviews*, *216*(8), 119. https://doi.org/10.1007/s11214-020-00742-2
McFadden, J. P., Carlson, C. W., Larson, D., Ludlam, M., Abiad, R., Elliott, B., et al. (2008). The THEMIS ESA plasma instrument and in-flight calibration. *Space Science Reviews*, *141*(1–4), 277–302. https://doi.org/10.1007/s11214-008-9440-2
Millan, R., Sample, J., Sotirelis, T., McCarthy, M., Woodger, L., Shih, A. Y., et al. (2022). New missions for understanding electron microburst precipitation. In *44th cospar scientific assembly* (Vol. 44, p. 3327). Held 16–24 July.
Min, K., Liu, K., Bonnell, J. W., Breneman, A. W., Denton, R. E., Funsten, H. O., et al. (2015). Study of EMIC wave excitation using direct ion measurements. *Journal of Geophysical Research*, *120*(4), 2702–2719. https://doi.org/10.1002/2014JA020717
Miyoshi, Y., Hosokawa, S., Kurita, S.-I., Oyama, Y., Ogawa, S., Saito, I., et al. (2021). Penetration of MeV electrons into the mesosphere accompanying pulsating aurorae. *Scientific Reports*, *11*(1), 13724. https://doi.org/10.1038/s41598-021-92611-3
Miyoshi, Y., Shinohara, I., Takashima, T., Asamura, K., Higashio, N., Mitani, T., et al. (2018). Geospace exploration project ERG. *Earth Planets and Space*, *70*(1), 101. https://doi.org/10.1186/s40623-018-0862-0
Mourenas, D., Artemyev, A. V., Agapitov, O. V., Krasnoselskikh, V., & Mozer, F. S. (2015). Very oblique whistler generation by low-energy electron streams. *Journal of Geophysical Research*, *120*(5), 3665–3683. https://doi.org/10.1002/2015JA021135

Mourenas, D., Artemyev, A. V., Ripoll, J.-F., Agapitov, O. V., & Krasnoselskikh, V. V. (2012). Timescales for electron quasi-linear diffusion by parallel and oblique lower-band Chorus waves. *Journal of Geophysical Research*, *117*(A6), A06234. https://doi.org/10.1029/2012JA017717

Mourenas, D., Artemyev, A. V., Zhang, X. J., Angelopoulos, V., Tsai, E., & Wilkins, C. (2021). Electron lifetimes and diffusion rates inferred from ELFIN measurements at low altitude: First results. *Journal of Geophysical Research: Space Physics*, *126*(11), e29757. https://doi.org/10.1029/2021JA029757

Ni, B., Cao, X., Zou, Z., Zhou, C., Gu, X., Bortnik, J., et al. (2015). Resonant scattering of outer zone relativistic electrons by multiband EMIC waves and resultant electron loss time scales. *Journal of Geophysical Research*, *120*(9), 7357–7373. https://doi.org/10.1002/2015JA021466

Ni, B., Thorne, R. M., Meredith, N. P., Shprits, Y. Y., & Horne, R. B. (2011). Diffuse auroral scattering by whistler mode chorus waves: Dependence on wave normal angle distribution. *Journal of Geophysical Research*, *116*(A10), 10207. https://doi.org/10.1029/2011JA016517

Ni, B., Thorne, R. M., Shprits, Y. Y., & Bortnik, J. (2008). Resonant scattering of plasma sheet electrons by whistler-mode chorus: Contribution to diffuse auroral precipitation. *Geophysical Research Letters*, *35*(11), 11106. https://doi.org/10.1029/2008GL034032

Nitta, N. V., Mulligan, T., Kilpua, E. K. J., Lynch, B. J., Mierla, M., O'Kane, J., et al. (2021). Correction to: Understanding the origins of problem geomagnetic storms associated with "StealthJin22: chorusshock coronal mass ejections. *Space Science Reviews*, *217*(Issue 8), 82. https://doi.org/10.1007/s11214-021-00860-5

O'Brien, T. P., Looper, M. D., & Blake, J. B. (2004). Quantification of relativistic electron microburst losses during the GEM storms. *Geophysical Research Letters*, *31*(4), L04802. https://doi.org/10.1029/2003GL018621

Omura, Y. (2021). Nonlinear wave growth theory of whistler-mode chorus and hiss emissions in the magnetosphere. *Earth Planets and Space*, *73*(1), 95. https://doi.org/10.1186/s40623-021-01380-w

Paschmann, G., Øieroset, M., & Phan, T. (2013). In-situ observations of reconnection in space. *Space Science Reviews*, *178*(2–4), 385–417. https://doi.org/10.1007/s11214-012-9957-2

Paschmann, G., Papamastorakis, I., Sckopke, N., Haerendel, G., Sonnerup, B. U. O., Bame, S. J., et al. (1979). Plasma acceleration at the earth's magnetopause – Evidence for reconnection. *Nature*, *282*(5736), 243–246. https://doi.org/10.1038/282243a0

Pettit, J., Elliott, S., Randall, C., Halford, A., Jaynes, A., & Garcia-Sage, K. (2023). Investigation of the drivers and atmospheric impacts of energetic electron precipitation. *Frontiers in Astronomy and Space Sciences*, *10*, 1162564. https://doi.org/10.3389/fspas.2023.1162564

Phan, T. D., Drake, J. F., Shay, M. A., Gosling, J. T., Paschmann, G., Eastwood, J. P., et al. (2014). Ion bulk heating in magnetic reconnection exhausts at Earth's magnetopause: Dependence on the inflow Alfvén speed and magnetic shear angle. *Geophysical Research Letters*, *41*(20), 7002–7010. https://doi.org/10.1002/2014GL061547

Richardson, I. G. (2018). Solar wind stream interaction regions throughout the heliosphere. *Living Reviews in Solar Physics*, *15*(1), 1. https://doi.org/10.1007/s41116-017-0011-z

Ross, J. P. J., Glauert, S. A., Horne, R. B., & Meredith, N. P. (2022). The importance of ion composition for radiation belt modeling. *Journal of Geophysical Research: Space Physics*, *127*(9), e30680. https://doi.org/10.1029/2022JA030680

Sagdeev, R. Z., & Shafranov, V. D. (1961). On the instability of a plasma with an anisotropic distribution of velocities in a magnetic field. *Soviet Physics – JETP*, *12*(1), 130–132.

Sanchez, E. R., Ma, Q., Xu, W., Marshall, R. A., Bortnik, J., Reyes, P., et al. (2022). A test of energetic particle precipitation models using simultaneous incoherent scatter radar and Van Allen Probes observations. *Journal of Geophysical Research: Space Physics*, *127*(8), e30179. https://doi.org/10.1029/2021JA030179

Sauer, K., Baumgaerte, K., & Sydora, R. D. (2020). Gap formation around $\omega_e/2$ and generation of low-band whistler waves by landau-resonant electrons in the magnetosphere: Predictions from dispersion theory. *Earth and Planetary Physics*, *4*, 138. https://doi.org/10.26464/epp2020020

Schulz, M., & Lanzerotti, L. J. (1974). *Particle diffusion in the radiation belts*. Springer.

Seon, J., Chae, K. S., Na, G. W., Seo, H. K., Shin, Y. C., Woo, J., et al. (2020). Particle detector (PD) experiment of the Korea space environment monitor (KSEM) aboard geostationary satellite GK2A. *Space Science Reviews*, *216*(1), 13. https://doi.org/10.1007/s11214-020-0636-4

Sheeley, B. W., Moldwin, M. B., Rassoul, H. K., & Anderson, R. R. (2001). An empirical plasmasphere and trough density model: CRRES observations. *Journal of Geophysical Research*, *106*(A11), 25631–25642. https://doi.org/10.1029/2000JA000286

Shen, Y., Chen, L., Zhang, X.-J., Artemyev, A., Angelopoulos, V., Cully, C. M., et al. (2021). Conjugate observation of magnetospheric chorus propagating to the ionosphere by ducting. *Geophysical Research Letters*, *48*(23), e95933. https://doi.org/10.1029/2021GL095933

Shue, J.-H., Chao, J. K., Fu, H. C., Russell, C. T., Song, P., Khurana, K. K., & Singer, H. J. (1997). A new functional form to study the solar wind control of the magnetopause size and shape. *Journal of Geophysical Research*, *102*(A5), 9497–9512. https://doi.org/10.1029/97JA00196

Shumko, M., Blum, L. W., & Crew, A. B. (2021). Duration of individual relativistic electron microbursts: A probe into their scattering mechanism. *Geophysical Research Letters*, *48*(17), e93879. https://doi.org/10.1029/2021GL093879

Silin, I., Mann, I. R., Sydora, R. D., Summers, D., & Mace, R. L. (2011). Warm plasma effects on electromagnetic ion cyclotron wave MeV electron interactions in the magnetosphere. *Journal of Geophysical Research: Space Physics*, *116*(A5), A05215. https://doi.org/10.1029/2010JA016398

SOSMAG. (2024). GEO-KOMPSAT-2A data base [Dataset]. https://swe.ssa.esa.int/

Stix, T. H. (1962). The theory of plasma waves.

Summers, D., Ni, B., & Meredith, N. P. (2007a). Timescales for radiation belt electron acceleration and loss due to resonant wave-particle interactions: 1. Theory. *Journal of Geophysical Research*, *112*(A4), 4206. https://doi.org/10.1029/2006JA011801

Summers, D., Ni, B., & Meredith, N. P. (2007b). Timescales for radiation belt electron acceleration and loss due to resonant wave-particle interactions: 2. Evaluation for VLF chorus, ELF hiss, and electromagnetic ion cyclotron waves. *Journal of Geophysical Research*, *112*(A4), 4207. https://doi.org/10.1029/2006JA011993

Summers, D., & Thorne, R. M. (2003). Relativistic electron pitch-angle scattering by electromagnetic ion cyclotron waves during geomagnetic storms. *Journal of Geophysical Research*, *108*(A4), 1143. https://doi.org/10.1029/2002JA009489

SUPERMAG. (2024). SUPERMAG data base of Sym-H and AE indexes [Dataset]. https://supermag.jhuapl.edu/

Tao, X., Zonca, F., Chen, L., & Wu, Y. (2020). Theoretical and numerical studies of chorus waves: A review. *Science China Earth Sciences*, *63*(1), 78–92. https://doi.org/10.1007/s11430-019-9384-6

THEMIS. (2024). Time history of events and macroscale interactions during substorms (THEMIS) mission data base [Dataset]. http://themis.ssl.berkeley.edu

Thorne, R. M., & Kennel, C. F. (1971). Relativistic electron precipitation during magnetic storm main phase. *Journal of Geophysical Research*, *76*(19), 4446–4453. https://doi.org/10.1029/JA076i019p04446

Tsai, E., Artemyev, A., Zhang, X.-J., & Angelopoulos, V. (2022). Relativistic electron precipitation driven by nonlinear resonance with whistler-mode waves. *Journal of Geophysical Research: Space Physics*, *127*(5), e30338. https://doi.org/10.1029/2022JA030338

Tsurutani, B. T., Gonzalez, W. D., Gonzalez, A. L. C., Guarnieri, F. L., Gopalswamy, N., Grande, M., et al. (2006). Corotating solar wind streams and recurrent geomagnetic activity: A review. *Journal of Geophysical Research*, *111*(A7), A07S01. https://doi.org/10.1029/2005JA011273

Tsurutani, B. T., Gonzalez, W. D., Gonzalez, A. L. C., Tang, F., Arballo, J. K., & Okada, M. (1995). Interplanetary origin of geomagnetic activity in the declining phase of the solar cycle. *Journal of Geophysical Research*, *100*(A11), 21717–21734. https://doi.org/10.1029/95JA01476

Tsurutani, B. T., Gonzalez, W. D., Guarnieri, F. o., Kamide, Y., Zhou, X., & Arballo, J. K. (2004). Are high-intensity long-duration continuous AE activity (HILDCAA) events substorm expansion events? *Journal of Atmospheric and Solar-Terrestrial Physics*, *66*(2), 167–176. https://doi.org/10.1016/j.jastp.2003.08.015

Tsurutani, B. T., Gonzalez, W. D., Lakhina, G. S., & Alex, S. (2003). The extreme magnetic storm of 1–2 September 1859. *Journal of Geophysical Research: Space Physics*, *108*(A7), 1268. https://doi.org/10.1029/2002JA009504

Tsurutani, B. T., Lakhina, G. S., Verkhoglyadova, O. P., Gonzalez, W. D., Echer, E., & Guarnieri, F. L. (2011). A review of interplanetary discontinuities and their geomagnetic effects. *Journal of Atmospheric and Solar-Terrestrial Physics*, *73*(1), 5–19. https://doi.org/10.1016/j.jastp.2010.04.001

Turunen, E., Kero, A., Verronen, P. T., Miyoshi, Y., Oyama, S.-I., & Saito, S. (2016). Mesospheric ozone destruction by high-energy electron precipitation associated with pulsating aurora. *Journal of Geophysical Research: Atmospheres*, *121*(19), 11852–11861. https://doi.org/10.1002/2016JD025015

Ukhorskiy, A. Y., Shprits, Y. Y., Anderson, B. J., Takahashi, K., & Thorne, R. M. (2010). Rapid scattering of radiation belt electrons by storm-time EMIC waves. *Geophysical Research Letters*, *37*(9), L09101. https://doi.org/10.1029/2010GL042906

Ukhorskiy, A. Y., Sitnov, M. I., Merkin, V. G., Gkioulidou, M., & Mitchell, D. G. (2017). Ion acceleration at dipolarization fronts in the inner magnetosphere. *Journal of Geophysical Research*, *122*(3), 3040–3054. https://doi.org/10.1002/2016JA023304

Ukhorskiy, A. Y., Sorathia, K. A., Merkin, V. G., Crabtree, C., Fletcher, A. C., Malaspina, D. M., & Schwartz, S. J. (2022). Cross-scale energy cascade powered by magnetospheric convection. *Scientific Reports*, *12*(1), 4446. https://doi.org/10.1038/s41598-022-08038-x

Ukhorskiy, A. Y., Sorathia, K. A., Merkin, V. G., Sitnov, M. I., Mitchell, D. G., & Gkioulidou, M. (2018). Ion trapping and acceleration at dipolarization fronts: High-resolution MHD and test-particle simulations. *Journal of Geophysical Research: Space Physics*, *123*(7), 5580–5589. https://doi.org/10.1029/2018JA025370

Upadhyay, A., Kakad, B., Kakad, A., & Rawat, R. (2022). Effect of solar wind pressure and substorm linked particle injection on local time distribution of electromagnetic ion cyclotron waves. *Frontiers in Astronomy and Space Sciences*, *9*, 866023. https://doi.org/10.3389/fspas.2022.866023

Usanova, M. E., Mann, I. R., Bortnik, J., Shao, L., & Angelopoulos, V. (2012). THEMIS observations of electromagnetic ion cyclotron wave occurrence: Dependence on AE, SYMH, and solar wind dynamic pressure. *Journal of Geophysical Research*, *117*(A10), 10218. https://doi.org/10.1029/2012JA018049

Wang, D., & Shprits, Y. Y. (2019). On how high-latitude chorus waves tip the balance between acceleration and loss of relativistic electrons. *Geophysical Research Letters*, *46*(14), 7945–7954. https://doi.org/10.1029/2019GL082681

Wu, D. J., Chao, J. K., & Lepping, R. P. (2000). Interaction between an interplanetary magnetic cloud and the Earth's magnetosphere: Motions of the bow shock. *Journal of Geophysical Research*, *105*(A6), 12627–12638. https://doi.org/10.1029/1999JA000265

Xia, Z., Chen, L., Artemyev, A., Zhu, H., Jordanova, V. K., & Zheng, L. (2019). The effects of localized thermal pressure on equilibrium magnetic fields and particle drifts in the inner magnetosphere. *Journal of Geophysical Research: Space Physics*, *124*(7), 5129–5142. https://doi.org/10.1029/2018JA026043

Xu, W., Marshall, R. A., Tyssøy, H. N., & Fang, X. (2020). A generalized method for calculating atmospheric ionization by energetic electron precipitation. *Journal of Geophysical Research: Space Physics*, *125*(11), e28482. https://doi.org/10.1029/2020JA028482

Xue, Z., Yuan, Z., Yu, X., Deng, D., Huang, Z., & Raita, T. (2022). EMIC waves observed throughout the inner magnetosphere driven by abrupt enhancement of the solar wind pressure. *Geophysical Research Letters*, *49*(9), e98954. https://doi.org/10.1029/2022GL098954

Yan, Y., Yue, C., Ma, Q., Zhou, X.-Z., Zong, Q.-G., Fu, H., et al. (2023). Prompt appearance of large-amplitude emic waves induced by solar wind dynamic pressure enhancement and the subsequent relativistic electron precipitation. *Journal of Geophysical Research: Space Physics*, *128*(7), e2023JA031399. https://doi.org/10.1029/2023JA031399

Yin, Z.-F., Zhou, X.-Z., Hu, Z.-J., Yue, C., Zong, Q.-G., Hao, Y.-X., et al. (2022). Localized excitation of electromagnetic ion cyclotron waves from anisotropic protons filtered by magnetic dips. *Journal of Geophysical Research: Space Physics*, *127*(6), e30531. https://doi.org/10.1029/2022JA030531

Yu, X., Yuan, Z., Huang, Z., Xue, Z., & Zhao, Y. (2023). Effects of magnetic dips on the propagation of electromagnetic ion cyclotron waves. *Journal of Geophysical Research: Space Physics*, *128*(3), e2022JA031178. https://doi.org/10.1029/2022JA031178

Yue, C., Chen, L., Bortnik, J., Ma, Q., Thorne, R. M., Angelopoulos, V., et al. (2017). The characteristic response of whistler mode waves to interplanetary shocks. *Journal of Geophysical Research: Space Physics*, *122*(10), 10047–10057. https://doi.org/10.1002/2017JA024574

Zhang, X.-J., Angelopoulos, V., Mourenas, D., Artemyev, A., Tsai, E., & Wilkins, C. (2022). Characteristics of electron microburst precipitation based on high-resolution ELFIN measurements. *Journal of Geophysical Research: Space Physics*, *127*(5), e30509. https://doi.org/10.1029/2022JA030509

Zhang, X.-J., Artemyev, A., Angelopoulos, V., Tsai, E., Wilkins, C., Kasahara, S., et al. (2022). Superfast precipitation of energetic electrons in the radiation belts of the Earth. *Nature Communications*, *13*(1), 1611. https://doi.org/10.1038/s41467-022-29291-8

Zhang, X.-J., Li, W., Thorne, R. M., Angelopoulos, V., Bortnik, J., Kletzing, C. A., et al. (2016). Statistical distribution of EMIC wave spectra: Observations from Van Allen Probes. *Geophysical Research Letters*, *43*(24), 12. https://doi.org/10.1002/2016GL071158

Zhao, X. X., Zong, Q. G., Liu, J. J., Yue, C., Zhou, X. Z., Hao, Y. X., et al. (2022). Normal- and reversed-boomerang stripes on electron pitch angle distributions: Solar wind dynamic pressure effect. *Geophysical Research Letters*, *49*(2), e96526. https://doi.org/10.1029/2021GL096526

Zhao, Y., Zhu, H., & Chen, H. (2023). Expected emic wave generation and unexpected ms wave disruption in a magnetic dip. *Journal of Geophysical Research: Space Physics*, *128*(8), e2023JA031776. https://doi.org/10.1029/2023JA031776

Zhou, C., Li, W., Thorne, R. M., Bortnik, J., Ma, Q., An, X., et al. (2015). Excitation of dayside chorus waves due to magnetic field line compression in response to interplanetary shocks. *Journal of Geophysical Research: Space Physics*, *120*(10), 8327–8338. https://doi.org/10.1002/2015JA021530

Zhou, X., Gao, X., Chen, R., Lu, Q., Ke, Y., Ma, J., & Kong, Z. (2023). Direct observation of rising-tone chorus triggered by enhanced solar wind pressure. *Journal of Geophysical Research: Space Physics*, *128*(11), e2023JA031787. https://doi.org/10.1029/2023JA031787

Zhu, H., Chen, L., Artemyev, A. V., Zhang, X.-J., & Breneman, A. W. (2021). Superposed epoch analyses of electron-driven and proton-driven magnetic dips. *Geophysical Research Letters*, *48*(21), e94934. https://doi.org/10.1029/2021GL094934

Zuxiang, X., Yuan, Z., Yu, X., Huang, Z., & Deng, D. (2023). Enhanced solar wind dynamic pressure as a driver of low-energy proton temperature anisotropies and high-frequency emic waves. *Journal of Geophysical Research: Space Physics*, *128*(9), e2023JA031929. https://doi.org/10.1029/2023JA031929